# Vimentin Intermediate Filaments Stabilize Dynamic Microtubules by Direct Interactions

Laura Schaedel,[†,¶] Charlotta Lorenz,[†,¶] Anna V. Schepers,[†] Stefan Klumpp,[*,‡] and Sarah Köster[*,†]

†*Institute for X-Ray Physics, University of Göttingen, Friedrich-Hund-Platz 1, 37077 Göttingen, Germany*

‡*Institute for the Dynamics of Complex Systems, University of Göttingen, Friedrich-Hund-Platz 1, 37077 Göttingen, Germany*

¶*equal contribution*

E-mail: stefan.klumpp@phys.uni-goettingen.de; sarah.koester@phys.uni-goettingen.de

Phone: +49 (0)551 39 26942 ; +49 (0)551 39 29429

**Abstract**

The cytoskeleton determines cell mechanics and lies at the heart of important cellular functions. Growing evidence suggests that the manifold tasks of the cytoskeleton rely on the interactions between its filamentous components, known as actin filaments, intermediate filaments and microtubules. However, the nature of these interactions and their impact on cytoskeletal dynamics are largely unknown. Here, we show in a reconstituted in vitro system that vimentin intermediate filaments stabilize microtubules against depolymerization and support microtubule rescue. To understand these stabilizing effects, we directly measure the interaction forces between individual microtubules and vimentin filaments. Combined with numerical simulations, our observations provide detailed insight into the physical nature of the interactions and how they affect

microtubule dynamics. Thus, we describe an additional, direct mechanism for cells to establish the fundamental cross-talk of cytoskeletal components alongside linker proteins. Moreover, we suggest a novel strategy to estimate the binding energy of tubulin dimers within the microtubule lattice.

The cytoskeleton is a dynamic biopolymer scaffold present in all eukaryotic cells. Its manifold tasks depend on the fine-tuned interplay between the three filamentous components, actin filaments, microtubules and intermediate filaments (IFs).[1–6] For example, all three types of cytoskeletal polymers participate in cell migration, adhesion and division.[3–6] In particular, the interplay of IFs and microtubules makes and important contribution to cytoskeletal cross-talk, although the interaction mechanisms largely remain unclear.[1,7–18]

For instance, vimentin, one of the most abundant members of the IF family, forms closely associated parallel arrays with microtubules.[7,16,18] Depolymerization of the microtubule network leads to a collapse of vimentin IFs to the perinuclear region, further attesting their interdependent organization in cells.[9] Several studies suggest that in cells, microtubules associated with the vimentin IF network are particularly stable: They exhibit increased resistance to drug-induced disassembly[9] and enhanced directional persistence during directed cell migration,[18] and they are reinforced against lateral fluctuations.[17] Several proteins such as kinesin,[8,11] dynein,[13,15] plectin[1] and microtubule-actin cross-linking factor (MACF)[10,12] can mediate interactions between IFs and microtubules. These linker proteins may be involved in conferring microtubule stability in cells. However, the possibility that more fundamental, direct interactions may contribute to stabilizing microtubules remains unexplored. Such a mechanism could also explain the results of an in vitro study on dynamic microtubules embedded in actin networks: Depending on the network architecture, actin regulates microtubule dynamics and life time. In particular, unbranched actin filaments seem to prevent microtubule catastrophe, thus stabilizing them, though the exact interaction mechanism is not revealed.[19] In contrast to the cell experiments that showed a stabilization of microtubules by IFs, earlier work found that many IFs, including vimentin, contain tubulin binding sites

and that short peptides containing these binding sites inhibit microtubule polymerization in vitro.[14] Yet, it is unknown how this effect relates to fully assembled vimentin filaments.

Overall, there is substantial evidence for the importance of the interplay between IFs and microtubules in cells. However, the nature of their direct interactions and its impact on cytoskeletal dynamics remains elusive. Here, we study these interactions by combining in vitro observations of dynamic microtubules in presence of vimentin IFs with single filament interaction measurements and complementary numerical simulations. In stark contrast to Ref. 14, our observations and simulations of dynamic microtubules reveal a stabilizing effect by the surrounding vimentin IFs. Based on our experimental data, we also estimate the tubulin dimer binding energy within the microtubule lattice, which is a much sought-after parameter for understanding microtubule dynamic instability.[20–27] This value has previously only been determined by molecular dynamics simulations and kinetic modeling[20,22,27] or by using atomic force microscopy to indent stabilized microtubules.[24]

To study the influence of IFs on microtubule dynamics, we polymerize microtubules in the presence of vimentin IFs. Supplementary Fig. 1 shows the length distribution of the IFs during the first 45 mins of assembly. We image the microtubules by total internal reflection fluorescence (TIRF) microscopy as sketched in Fig. 1a. As nucleation sites for dynamic microtubules, we use GMPCPP-stabilized microtubule seeds (green in Fig. 1a) adhered to a passivated glass surface. For simultaneous assembly of microtubules (cyan) and IFs (red), we supplement a combined buffer (CB) containing all ingredients necessary for the assembly of both filament types with 20 µM or 25 µM tubulin and 2.3 µM vimentin tetramers (0.5 g/L protein). Fig. 1b shows a typical fluorescence image of mixed microtubules and vimentin IFs.

We analyze microtubule dynamics using kymographs obtained from TIRF microscopy as shown in Fig 1c. As expected,[28] the microtubule growth rate increases at the higher tubulin concentration (Fig. 1d, cyan), yet, the presence of vimentin IFs does not affect the growth rate. Interestingly, we observe a marked decrease in the catastrophe frequency[29] in presence

of vimentin IFs at both tubulin concentrations (Fig. 1e, red and cyan stripes). Moreover, vimentin IFs promote microtubule rescue (Fig. 1f). As rescue events are rare at the lower tubulin concentration,[29] we only report rescue data for 25 µM tubulin. These results indicate that vimentin IFs stabilize dynamic microtubules by suppressing catastrophe and enhancing rescue, while leaving the growth rate unaffected.

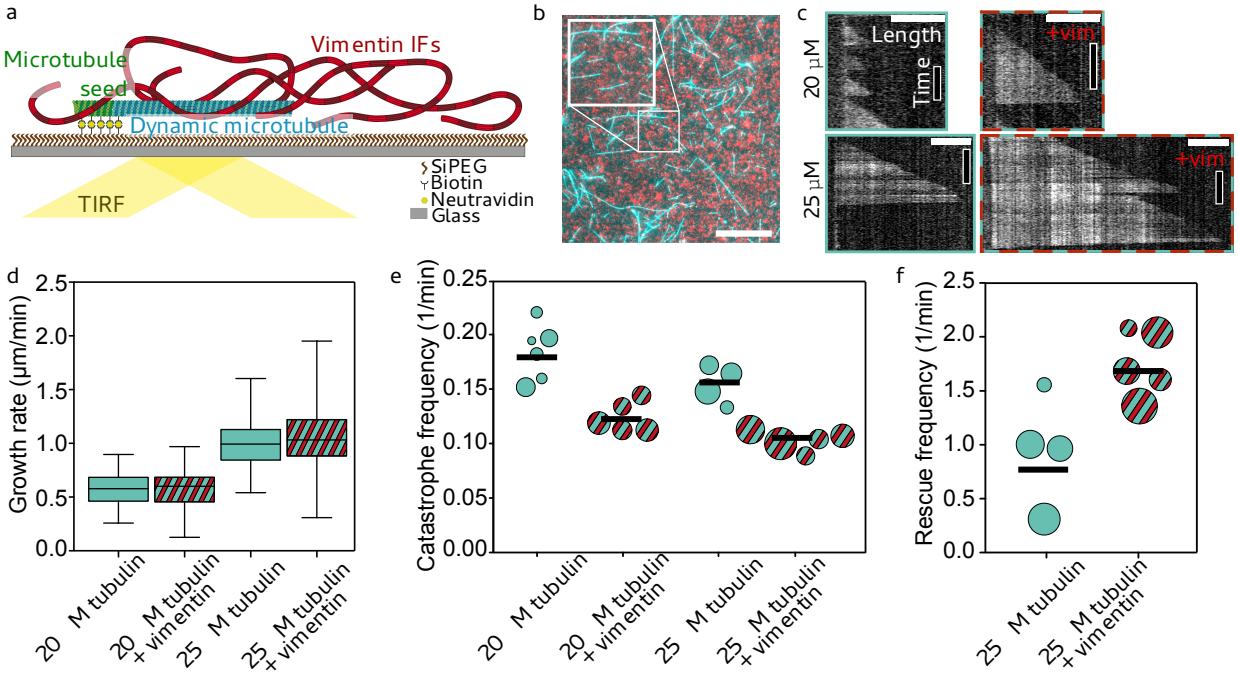


Figure 1: Vimentin IFs stabilize dynamic microtubules. (a) Illustration of the experimental setup. We attach microtubule seeds (green) to a biotin-SiPEG coated cover glass. Dynamic microtubules (cyan) grow from the seeds. Vimentin IFs (red) form an entangled, fluctuating network. We image microtubules by TIRF microscopy. (b) Fluorescence micrograph of microtubules (cyan) embedded in a vimentin IF network (red). Inset shows enlarged detail. Scale bar: 10 µm. (c) Example kymographs of microtubules growing at 20 µM or 25 µM tubulin in the presence (+vim) or absence of vimentin. Scale bars: 3 µm and 5 min. (d) Vimentin does not affect the microtubule growth rate, irrespective of the tubulin concentration. Cyan represents experiments with tubulin only, cyan and red stripes illustrate experiments with tubulin and vimentin. (e) The catastrophe frequency of microtubules decreases in the presence of vimentin. Each circle represents an experiment including multiple microtubules. The circle area scales with the total summed microtubule growth time of the respective experiment. Black bars indicate the weighted mean. (f) Vimentin enhances the microtubule rescue frequency. Each circle represents an experiment including multiple microtubules. The circle area scales with the total microtubule depolymerization time.

From these observations, we hypothesize that there are direct, attractive interactions

between microtubules and vimentin IFs, which stabilize dynamic microtubules. To test this hypothesis, we study the interactions of single stabilized microtubules and vimentin IFs with optical trapping (OT) as illustrated in Fig. 2. We prepare fluorescent and biotin-labeled microtubules and vimentin IFs as sketched in Supplementary Fig. 2. We use an OT setup, combined with a microfluidic device and a confocal microscope (LUMICKS, Amsterdam, The Netherlands) to attach a microtubule and a vimentin IF to separate bead pairs via biotin-streptavidin bonds as shown in Fig. 2a and Supplementary Fig. 3a. Once the IF and microtubule are in contact, we move the IF back and forth in $y$-direction. If the IF and microtubule interact, eventually either the IF-microtubule interaction breaks (Fig. 2b) or the IF-microtubule interaction is so strong that the microtubule breaks off a bead (Fig. 2c). We categorize the type of interaction, i.e. no interaction, IF-microtubule bond breaks, or microtubule breaks off bead, for each filament pair as shown by pictograms in Fig. 3a, top.

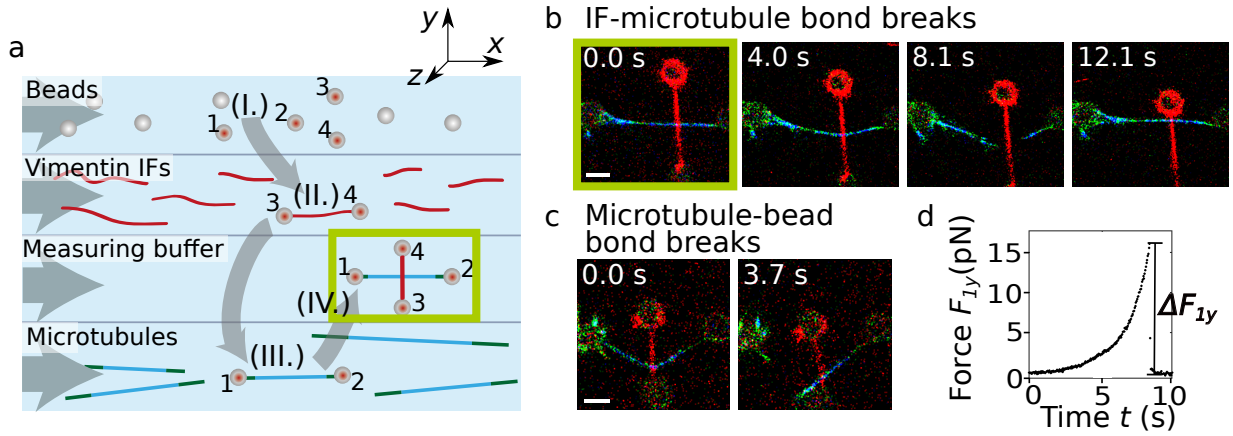


Figure 2: Direct interactions between stabilized microtubules and vimentin IFs. (a) Schematic of the setup for the OT experiments for interaction measurements in microfluidic flow channels. Four streptavidin-coated beads are captured by OTs (I.). We use one bead pair (beads 3 and 4) to attach a vimentin IF (II., red), and the other bead pair (beads 1 and 2) to attach a microtubule (III., green-cyan). We bring the IF and the microtubule into contact in a crossed configuration (IV.). Next, we move the IF perpendicularly to the microtubule to study the IF-microtubule interactions while we take confocal fluorescence images (starting position marked in light green in (a) and (b)). (b) Typical confocal fluorescence images of an IF-microtubule interaction which breaks and (c) a strong IF-microtubule interaction for which the microtubule breaks off the bead. Scale bars: 5 µm. (d) Typical experimental force increase $F_{1y}$ on bead 1 in the $y$-direction once a bond forms. Breaking of the force causes a force jump of $\Delta F_{1y}$.

With the OTs, we record the force $F_{1y}$ that acts on trap 1 in $y$-direction (see Fig. 2d and Supplementary Fig. 3b), which increases after the IF binds to the microtubule. Based on the geometry of the filament configuration from the confocal images, we calculate the total force that the IF exerts on the microtubule (see Supplementary Fig. 3c). In Fig. 3b we show the resulting force calculated for the data shown in Fig. 2d. Repetition of the experiment leads to a distribution of $n_i$ breaking forces as shown in the force histogram in Fig. 3c. The breaking forces are in the range of 1-65 pN with higher forces occurring less often. Hence, in agreement with our hypothesis, our experiments show that single microtubules and vimentin IFs directly interact, i.e. without involving any linker proteins, and that these interactions can become so strong that forces up to 65 pN are needed to break the bonds. This range of forces is physiologically relevant and comparable to other microtubule associated processes: Single microtubules can generate pushing forces of 3-4 pN while forces associated with depolymerization can reach 30-65 pN.[30] Kinesin motors have stalling forces on the order of a few pN.[31]

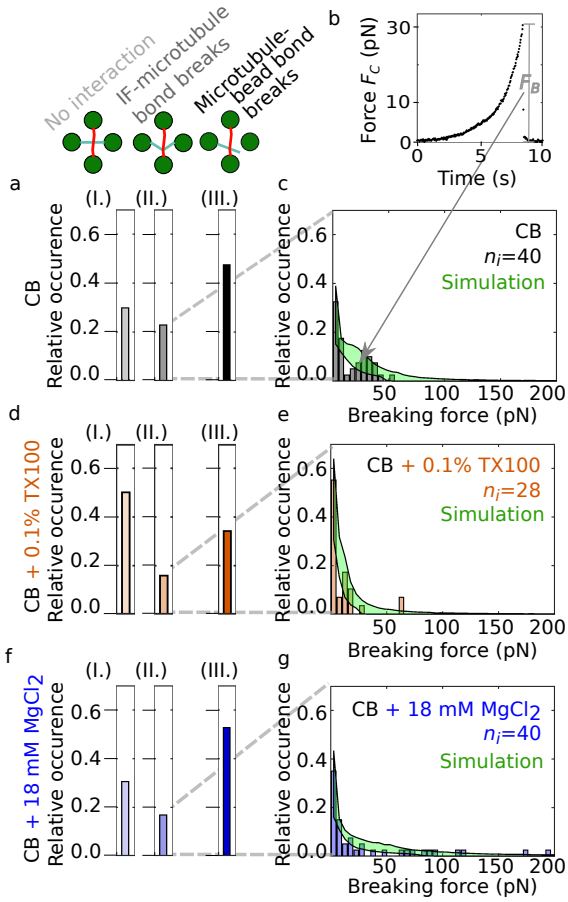


Figure 3: Hydrophobicity and electrostatics contribute to the IF-microtubule interactions. (a) We classify the interactions between IF-microtubule pairs into three different groups as shown by the pictograms: no interaction (I.), breaking of the IF-microtubule bond (II.), and breaking of the microtubule-bead bond (III.). (b) Typical experimental force-time behavior of the IF-microtubule bond showing the total force acting on the IF-microtubule bond. The plot represents the corrected version of the force data shown in Fig. 2d taking into account the geometry of the filament configuration. (c) Histograms of $n_i$ experimentally recorded breaking forces (gray) and simulated data (green) for measurements in pure CB. (d) TX100 (orange) suppresses some of the interactions, which results in more IF-microtubule pairs without any interaction (aI. vs. dI.) and fewer instances of IF-microtubule interactions (aII.-III. vs. dII.-III.). (e) The IF-microtubule bonds formed in presence of TX100 break at lower forces. (f) Magnesium (blue) does not change the relative number of IF-microtubule pairs which do not interact (aI. vs. fI.), but leads to fewer IF-microtubule breaking events (aII. vs. fII.) because the interactions become so strong that the microtubule breaks off the bead more often (aIII. vs. fIII.). (g) The IF-microtubule bonds formed in presence of additional magnesium break at higher forces.

To better understand the nature of the interactions between single microtubules and vimentin IFs, we vary the buffer conditions in which we measure filament interactions. First, we

probe possible hydrophobic contributions to the interactions by adding 0.1% (w/v) Triton-X 100 (TX100), a non-ionic aqueous detergent. Rheological studies of IF networks previously suggested that TX100 inhibits hydrophobic interactions.[32] Tubulin dimers have several hydrophobic regions as well,[33] some of which are accessible in the assembled state.[34] As shown in Fig. 3d and e, the number of interactions decreases and the breaking forces are slightly lower in presence of TX100 than in pure CB. We calculate the binding rate $r_{b,\mathrm{eff}}$ by dividing the total number of interactions by the time for which the two filaments are unbound: TX100 leads to a lower binding rate $r_{b,\mathrm{eff,TX100}} = 0.56 \cdot 10^{-2}$ s$^{-1}$ compared to the binding rate $r_{b,\mathrm{eff}} = 1.1 \cdot 10^{-2}$ s$^{-1}$ without TX100. We speculate that TX100 interferes with the binding sites on both filament types by occupying hydrophobic residues on the surface of the filaments and thereby inhibits hydrophobic interactions between the biopolymers.[32] Consequently, the reduced number of interactions in presence of TX100 indicates that hydrophobic effects contribute to the interactions.

Next, we test for electrostatic contributions to the interactions by adding magnesium chloride to the buffer. When probing interactions in CB buffer with a total concentration of 20 mM magnesium, we observe both an increase in strong interactions, where the IF pulls the microtubule off a bead, and higher breaking forces (3aIII. vs. fIII. and c vs. g). The binding rate of microtubules and vimentin IFs increases to $r_{b,\mathrm{eff,Mg}} = 1.3 \cdot 10^{-2}$ s$^{-1}$. Generally, charged, suspended biopolymers in the presence of oppositely charged multivalent ions have been shown to attract these ions, leading to counterion condensation along the biopolymers. Consequently, the filaments attract each other through overscreening.[35,36] Our data are in agreement with this effect. At high magnesium concentration, bonds form more likely and become stronger. Therefore, we conclude that both hydrophobic and electrostatic effects contribute to the direct interactions between microtubules and vimentin IFs.

For a more profound understanding of how these reagents change the physical bond parameters, which are not accessible experimentally, we apply a modeling approach. We model the IF-microtubule interaction as a single molecular bond with force-dependent stochastic

transitions between the bound and unbound state. The time-dependent force increase $F(t)$ has an entropic stretching contribution[37,38] for forces below 5 pN and increases linearly for higher forces as observed in the experiment.[39,40] We assume that the binding ($b$) and unbinding ($u$) rates $r_b$ and $r_u$, respectively, depend on the applied force, an activation energy $E_{Ab}$ or $E_{Au}$, the thermal energy $k_BT$ and a distance $x_b$ or $x_u$ to the transition state, which is on the order of the distance between the IF and the microtubule at the site of the bond:

$$r_b(t) = r_{b,0} \exp\left(\frac{-E_{Ab}}{k_BT}\right) \cdot \exp\left(\frac{-F(t)x_b}{k_BT}\right), r_u(t) = r_{u,0} \exp\left(\frac{-E_{Au}}{k_BT}\right) \cdot \exp\left(\frac{F(t)x_u}{k_BT}\right). \quad (1)$$

We summarize the force independent factor in Eq. (1) as an effective zero-force rate:

$$r_{b,\mathrm{eff}/u,\mathrm{eff}} = r_{b,0/u,0} \exp\left(\frac{-E_{Ab/Au}}{k_BT}\right). \quad (2)$$

In contrast to the force and the effective binding rate $r_{b,\mathrm{eff}}$, neither $r_{u,\mathrm{eff}}$ nor $x_b$ or $x_u$ can be determined from our experimental data. Due to detailed balance, the sum $x_b + x_u$ is constant.[41] Since we only observe a small number of rebinding events under force, we focus on the unbinding processes and study $x_u$. Hence, we simulate IF-microtubule interactions for different sets of $r_{u,\mathrm{eff}}$ and $x_u$ and compare the resulting distributions of breaking forces to our experimental data. We accept the tested parameter sets if the distributions pass the Kolmogorov-Smirnov test with a significance level of 5%. The minimum and maximum of all accepted simulation results, shown as the borders of the green areas in Fig. 3c, e and g, agree well with the experiments. Fig. 4a shows all accepted parameter pairs $r_{u,\mathrm{eff}}$ and $x_u$ for the different buffer conditions (color code: gray (pure CB), orange (CB with TX100), blue (CB with additional magnesium); corresponding mixed colors for regions, where valid parameters overlap). Both parameters increase from additional magnesium (blue) across no addition (gray) to added TX100 (orange). To understand these data more intuitively, we calculate the energy diagrams, as plotted in Fig. 4b, using Eq. (9) (see Materials and

Methods) considering the same buffer condition in unbound and bound (1 and 2) state or different buffer conditions (1 and 2) and the same state.

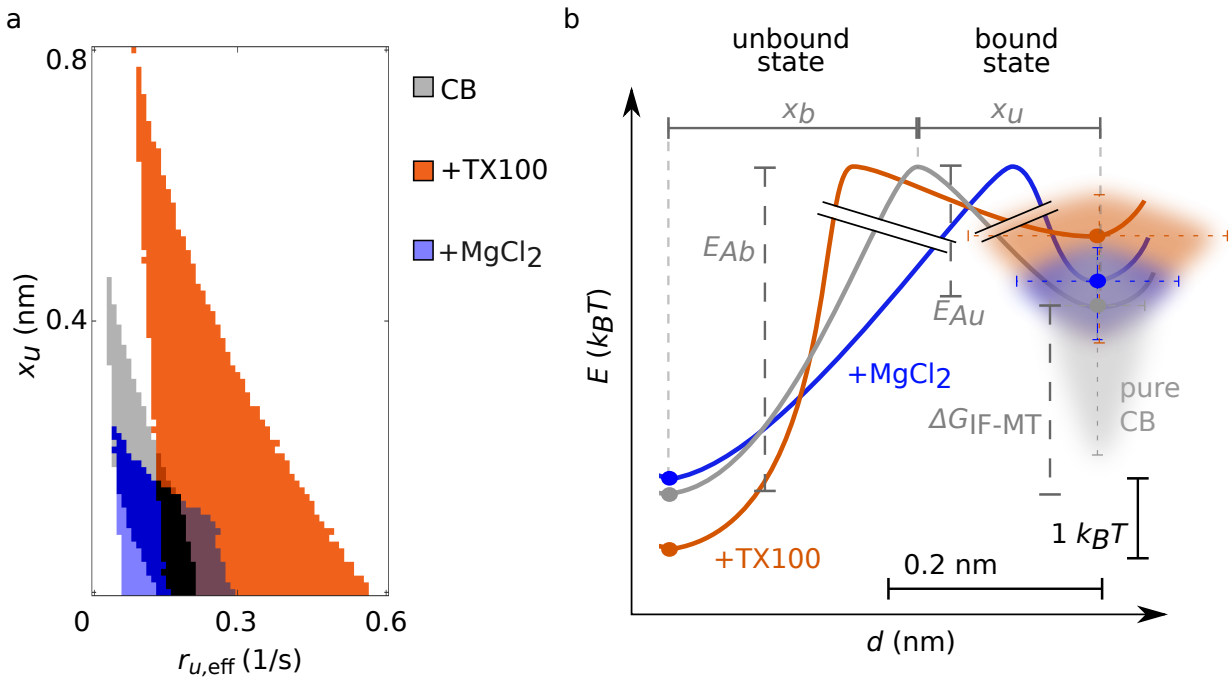


Figure 4: Hydrophobic and ionic reagents change the IF-microtubule bond properties. (a) Valid unbinding rates $r_{u,\mathrm{eff}}$ and potential widths $x_u$ to simulate the experimental data shown in Fig. 3c, e and g for the different buffer conditions: pure CB (gray), CB with TX100 (orange) and CB with additional magnesium (blue). $r_{u,\mathrm{eff}}$ and $x_u$ pairs, which are valid for several buffer conditions, are color coded by mixed colors. $r_{u,\mathrm{eff}}$ and $x_u$ increase from additional magnesium chloride across pure CB to added TX100. (b) Energy landscape for the theoretical modeling of the IF-microtubule bond: A two-state model (unbound, bound) is sufficient to describe the experimental data shown in Fig. 3. From the binding and unbinding rates, we can calculate the differences in activation energies, $E_{Ab}$ and $E_{Au}$, see Eq. (9), of bonds in different buffer conditions to open or close. However, the absolute values cannot be determined, as indicated by the graph break (black double-lines). For different buffer conditions, the position of the energy barrier relative to the unbound and bound state, $x_b$ and $x_u$, respectively, changes.

Surprisingly, both TX100 and additional magnesium only mildly affect the activation energies. Yet, for TX100 we observe a marked increase in distance to the transition state, $x_u$ (compare Fig. 4b orange to gray), which we interpret as a "looser binding" between the IF and the microtubule. Thus the force-dependent term in Eq. (1) becomes more pronounced. TX100 can interact with hydrophobic residues and forces the filaments to stay further apart.

Thus, the bond breaks at lower forces. Consequently, this further confirms that there is a hydrophobic contribution to the interactions in CB.

In contrast to TX100, magnesium acts as a divalent counterion between two negative charges, further strengthening the bond and keeping it closed even at higher forces. It lowers the distance to the transition state (compare Fig. 4b blue to gray) and the influence of the force-dependent term in Eq. (1). Hence, the opening of the bond depends less on the applied force compared to bonds in pure CB. Since CB already includes 2 mM magnesium, we assume that there is an electrostatic contribution to the interactions observed in CB as well.

We have shown that there are hydrophobic and electrostatic contributions to the interactions between IFs and microtubules and we have derived key parameters of these interactions by combining experiments with theoretical modeling. To better understand how these interactions lead to the observed changes in microtubule dynamics, we again apply a modeling approach. We consider a microtubule as a dynamic lattice with GTP and GPD dimers[20,26] as sketched in Fig. 5a. The lattice consists of 13 protofilaments and has a seam between the first and 13th protofilament. We describe the microtubule dynamics by three reactions: (i) A GTP dimer associates with a rate $r_g$, (ii) a GTP dimer is hydrolyzed with a rate $r_{hy}$, or (iii) a GDP or GTP dimer dissociates with a rate $r_{dd}$ or $r_{dt}$, respectively, which depends on the number of neighboring dimers, see Eq. (13) in Materials and Methods. A snapshot of the simulated microtubule during growth is shown in Fig. 5b. With a Monte-Carlo simulation, we obtain typical simulated kymographs (Fig. 5c). As for the experiments (semi-transparent data in Fig. 5d-f), we determine the growth rate, the catastrophe and the rescue frequency from the simulations (opaque in Fig. 5d-f).

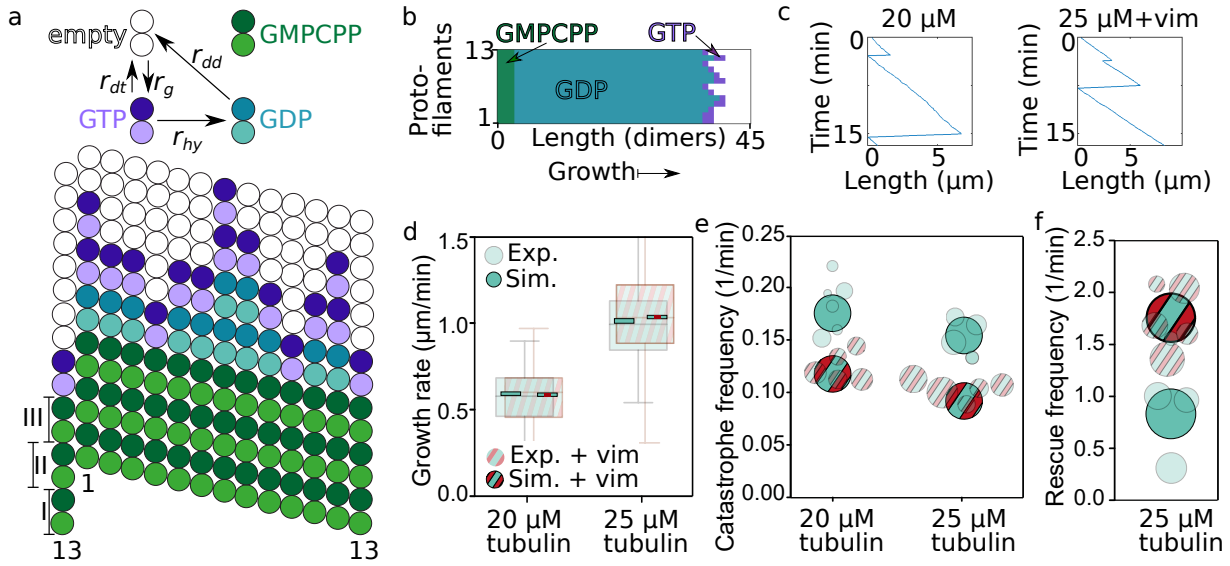


Figure 5: A Monte-Carlo simulation shows that temporarily binding IFs stabilize dynamic microtubules. (a) Illustration of the reaction rates (top) and simulated microtubule lattice with 13 protofilaments and a seam with a longitudinal displacement of 1.5 dimers (bottom). (b) Typical simulated microtubule growing from a GMPCPP seed with dimers either in the GTP (purple) or GDP state (cyan). (c) Typical length-time plot (kymograph) of a simulated microtubule in 20 µM free tubulin solution without vimentin tetramers (left) or in 25 µM free tubulin solution with vimentin tetramers (right). (d-f) We reproduce the experimental data shown in Fig. 1d-f (shown here in a semi-transparent fashion) with our Monte-Carlo simulation (opaque). (d) Addition of vimentin neither changes experimental nor simulated microtubule growth rates at 20 or 25 µM. For clarity, the complete standard deviation of the experimental data is not shown, but presented in Fig. 1. (e) Addition of vimentin lowers the catastrophe frequency of dynamic microtubules for both tubulin concentrations studied here. (f) In case of 25 µM free tubulin, the rescue rate increases due to the stabilizing effect of surrounding vimentin IFs. The circle areas scale with the total microtubule depolymerization time as in the representation of the experimental data.

To simulate microtubules in the presence of vimentin IFs, we consider the interactions of IFs and microtubules measured with OT experiments again. We calculate the approximate binding energy of microtubules and vimentin IFs from the effective binding and unbinding rates extracted from the OT experiments and simulations, see Eq. (10), to be $\Delta G_{\text{IF-MT}} = 2.3$ $k_B T$ as sketched in Fig. 4b. We apply this value and the viscosity of the liquid as well as the vimentin filament length (see Supplementary Fig. 1) used in the TIRF experiments to the simulated dynamic microtubules. We assume that IFs stochastically bind to individual tubulin dimers in the microtubule lattice, thus, stabilizing them by increasing their total binding

energy in the lattice by 2.3 $k_BT$. In agreement with our experimental data, the transient binding of IFs leaves the growth rate unaffected. Intriguingly, we observe that IF binding to tubulin dimers in the lattice reduces the catastrophe frequency. The increased binding energy of a dimer also raises the rescue frequency. These results are in striking agreement with our observation in TIRF experiments, while the only additional input to the simulation that includes the surrounding vimentin IFs are the parameters from OT experiments. Thus, stochastic, transient binding of IFs to microtubules as in the OT experiments is sufficient to explain the observed changes in microtubule dynamics in presence of IFs.

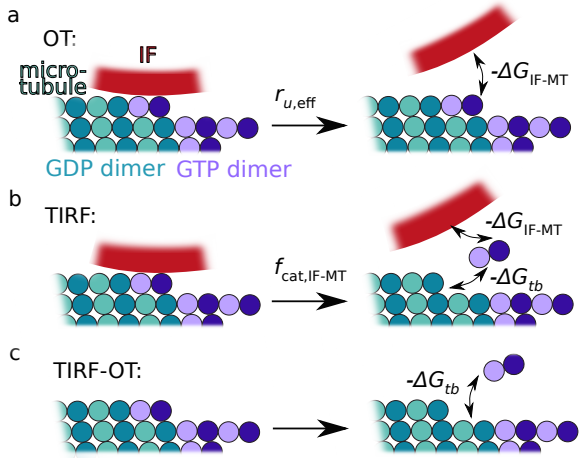


Figure 6: We estimate the binding energy of a single tubulin dimer by combining our OT and TIRF experiments. (a) From the OT experiments including the simulations, we determine the unbinding rate of microtubules and vimentin IFs $r_{u,\mathrm{eff}}$ and the released energy $-\Delta G_{\mathrm{IF\text{-}MT}}$ during unbinding. (b) In TIRF experiments, a tubulin dimer dissociates from the microtubule and the vimentin IF, so that the total energy $-\Delta G_{tb} - \Delta G_{\mathrm{IF\text{-}MT}}$ is released. We calculate the catastrophe frequency of a microtubule $f_{\mathrm{cat,IF\text{-}MT}}$ in case a vimentin IF is bound to the microtubule. (c) We estimate the average binding energy $\Delta G_{tb}$ of a tubulin dimer in the microtubule lattice before catastrophe by subtracting the released energies from (b) $(-\Delta G_{tb} - \Delta G_{\mathrm{IF\text{-}MT}})$ and by dividing the unbinding rate $r_{u,\mathrm{eff}}$ of microtubules and vimentin IFs by the catastrophe frequency $f_{\mathrm{cat,IF\text{-}MT}}$ of microtubules bound to a vimentin IF as in Eq. (16) in Materials and Methods.

By combining the results from OT and TIRF experiments, we estimate the total binding energy of a tubulin dimer within the lattice at the microtubule tip before catastrophe. From the OT experiments, including the corresponding simulations, we calculate the IF-microtubule bond energy $\Delta G_{\mathrm{IF\text{-}MT}} = 2.3\ k_BT$ and the unbinding rate $r_{u,\mathrm{eff}}$ of microtubules

and vimentin IFs (Fig. 6a). From the TIRF experiments, we determine the catastrophe frequency $f_{\text{cat,IF-MT}}$ of a microtubule bound to a vimentin IF. At the beginning of the catastrophe, a vimentin IF unbinds from the tubulin dimer, so that the energy $\Delta G_{\text{IF-MT}}$ is released. Simultaneously, the dimer depolymerizes from the lattice and the energy $\Delta G_{tb}$ is set free (Fig. 6b). The only additional energy released during microtubule catastrophe in TIRF experiments compared to the OT experiments is the binding energy to the surrounding tubulin dimers (Fig. 6c). Thus, comparing the rates of IF-microtubule unbinding and microtubule catastrophe during binding to a vimentin IF as in Eq. (16) in Materials and Methods, results in an estimation of the average tubulin binding energy $\Delta G_{tb} = 5.1\ k_BT$ and $5.2\ k_BT$ in the lattice at the tip for 20 and 25 µM tubulin concentration, respectively. These values for $\Delta G_{tb}$ are on the order of magnitude expected from literature.[20,27] To the best of our knowledge, there is no other experimental value available of the tubulin dimer binding energy in the non-stabilized microtubule lattice. Thus, from a broader perspective, our combination of experiments is a general approach to determine such binding energies and could be transferred to all proteins which bind to microtubules.

Our study examines interactions between microtubules and vimentin IFs. We show that vimentin IFs stabilize microtubules by direct interactions, which is in strong contrast to previous findings,[14] where, however, only interactions between microtubules and short IF peptides were considered. Whereas the microtubule growth rate remains unchanged, the stabilization by vimentin IFs leads to a reduction in the catastrophe frequency and increased rescue of depolymerizing microtubules. We pinpoint the source of this stabilizing effect to a stochastic, transient binding of IFs to microtubules by directly measuring the interactions of single filaments. Both hydrophobic and electrostatic effects are involved in bond formation. The presence of cations likely contributes to the attractive interactions between the negatively charged filaments. The buffer in which we conduct the measurements contains potassium and magnesium, two of the most abundant cations in cells.[42] The free magnesium concentration is on the order of a few mM in most mammalian cells,[43] similar to our exper-

iments. Magnesium ions have been previously described to cross-link vimentin IFs,[44–48] and we show that it can modulate the IF-microtubule bond strength. Since our magnesium concentrations are close to physiological values, the magnesium induced IF-microtubule binding we observe may occur in cells as well. Therefore, although molecular motors and cross-linkers contribute to establishing links between IFs and microtubules in cells, it is possible that more fundamental, direct attractive interactions also participate in the crosstalk of the two cytoskeletal subsystems in cells. The interactions we observe might thus be linked to cytoskeletal phenomena observed in cells such as the coalignment of microtubules and vimentin IFs in migrating epithelial cells[18] and the coexistensive network formation in migrating astrocytes.[16] There is growing evidence that a mechanical coupling between the cytoskeletal subsystems is necessary for many cellular functions such as polarization, migration and mechanical resistance.[2,49,50] In particular, vimentin deficient cells exhibit a less robust microtubule network orientation[18] and stronger microtubule fluctuations,[17] and they show impaired migration, contractility and resistance to mechanical stress.[51–53] Therefore, future research might help to explore the implications of our findings for cell mechanics and function. Furthermore, our study fosters understanding of emergent material properties of hybrid networks composed of cytoskeletal filaments and provides a basis for interpreting rheology data. Our combination of experiments also offers a new approach to estimate the tubulin bond energy within the microtubule lattice, which is a vital parameter to understand microtubule dynamics, mechanics and function.[20–27]

# Materials and Methods

## Vimentin purification, labeling and assembly

Vimentin C328N with two additional glycines and one additional cysteine at the C-terminus is recombinantly expressed as previously described[54–56] and stored at -80°C in 1 mM EDTA, 0.1 mM EGTA, 0.01 M MAC, 8 M urea, 0.15-0.25 M potassium chloride and 5 mM TRIS

at pH 7.5.[56] After thawing, we label the vimentin monomers with the fluorescent dye ATTO647N (AD 647N-41, AttoTech, Siegen, Germany) and with biotin via malemeide (B1267-25MG, Jena Bioscience, Jena, Germany) as described in Refs. 57–59. We mix labeled and unlabeled vimentin monomers, so that in total 4% of all monomers are fluorescently labeled, a maximum of 20 % is biotin labeled and all other monomers are unlabeled.[55,59] We reconstitute vimentin tetramers by first dialyzing the protein to 6 M urea, 50 mM phoshate buffer (PB), pH 7.5, and then in a stepwise manner to 0 M urea (4, 2, 0 M urea) in 2 mM PB, pH 7.5,[60] followed by an additional dialysis step into 0 M urea, 2 mM PB, pH 7.5, overnight at 10°C. To assemble vimentin into filaments, we dialyze the protein into assembly buffer, i.e. 100 mM KCl, 2 mM PB, pH 7.5, at 36°C overnight.[56,60]

## Tubulin purification and labeling

We purify tubulin from fresh bovine brain by a total of three cycles of temperature-dependent assembly and disassembly in Brinkley buffer 80 (BRB80 buffer; 80 mM PIPES, 1 mM EGTA, 1 mM $MgCl_2$, pH 6.8, plus 1 mM GTP) as described in Ref. 61. After two cycles of polymerization and depolymerization, we obtain microtubule-associated protein (MAP)-free neurotubulin by cation-exchange chromatography (1.16882, EMD $SO_3$, Merck, Darmstadt, Germany) in 50 mM PIPES, pH 6.8, supplemented with 0.2 mM $MgCl_2$ and 1 mM EGTA.[62] We prepare fluorescent tubulin (ATTO488- and ATTO565-labeled tubulin; AttoTech AD488-35 and AD565-35, AttoTech) and biotinylated tubulin (NHS-biotin, 21338, Thermo Scientific, Waltham, Massachusetts, USA) as previously described.[63] In brief, microtubules are polymerized from neurotubulin at 37°C for 30 min, layered onto cushions of 0.1 M NaHEPES, pH 8.6, 1 mM $MgCl_2$, 1 mM EGTA 60% v/v glycerol, and sedimented by centrifugation at 250,000 × g 37°C for 1 h. We resuspend microtubules in 0.1 M Na-HEPES, pH 8.6, 1 mM $MgCl_2$,1 mM EGTA, 40 % v/v glycerol and label the protein by adding 1/10 volume 100 mM NHS-ATTO or NHS-biotin for 10 min at 37°C. We stop the labeling reaction by adding 2 volumes of BRB80x2, containing 100 mM potassium glutamate and 40% v/v glyc-

erol. Afterwards, we centrifuge microtubules through cushions of BRB80 containing 60% v/v glycerol. We resuspend microtubules in cold BRB80 and perform an additional cycle of polymerization and depolymerization before we snap-freeze the tubulin in liquid nitrogen and store it in liquid nitrogen until use.

## Microtubule seeds for TIRF epxeriments

We prepare microtubule seeds at 10 µM tubulin concentration (30% ATTO-565-labeled tubulin and 70% biotinylated tubulin) in BRB80 supplemented with 0.5 mM GMPCPP at 37°C for 1 h. We incubate the seeds with 1 µM taxol for 30 min at room temperature and then sediment them by centrifugation at 100,000 × g for 10 min at 37°C. We discard the supernatant and carefully resuspend the pellet in warm BRB80 supplemented with 0.5 mM GMPCPP and 1 µM taxol. We either use seeds directly or snap freeze them in liquid nitrogen and store them in liquid nitrogen until use.

## Sample preparation for optical trapping experiments

We prepare stabilized microtubules with biotinylated ends for optical trapping by first polymerizing the central part of the microtubules through step-wise increase of the tubulin concentration. Initially, a 3 µM tubulin (5% ATTO-488-labeled) solution in M2B buffer (BRB80 buffer supplemented with 1 mM $MgCl_2$) in the presence of 1 mM GMPCPP (NU-405L, Jena Bioscience) is prepared at 37°C to nucleate short microtubule seeds. Next, the concentration is increased to a total of 9 µM tubulin in order to grow long microtubules. To avoid further microtubule nucleation, we add 1 µM tubulin at a time from a 42 µM stock solution (5% ATTO-488-labeled) and wait 15 min between the successive steps. To grow biotinylated ends, we add a mix of 90% biotinylated and 10% ATTO-565-labeled tubulin in steps of 0.5 µM from a 42 µM stock solution up to a total tubulin concentration of 15 µM. We centrifuge polymerized microtubules for 10 min at 13000 × g to remove any non-polymerized tubu-

lin and short microtubules. We discard the supernatant and carefully resuspend the pellet in 800 µL M2B-taxol (M2B buffer supplemented with 10 µM taxol (T7402, Merck)). By keeping the central part of the microtubules biotin-free (see color code in Fig. 2a: biotin-free microtubule in cyan and biotin labeled microtubule ends in green), we ensure that any streptavidin molecules detaching from the beads cannot affect interaction measurements by cross-linking the filaments.

For measurements in the microfluidic chip by optical trapping, we prepare four solutions for the four different microfluidic channels as sketched in Fig. 2a: (I) We dilute streptavidin-coated beads with an average diameter of 4.5 µm (PC-S-4.0, Kisker, Steinfurt, Germany) 1:83 with vimentin assembly buffer. (II) We dilute the vimentin IFs 1:667 with vimentin assembly buffer. (III.) We dilute the resuspended microtubules 1:333 with CB. (IV.) We combine suitable buffer conditions for microtubules and for vimentin IFs, respectively, to a combination buffer (CB) containing 1 mM EGTA (03777, Merck), 2 mM magnesium chloride, 25 mM PIPES (9156.4, Carl Roth, Karlsruhe, Germany), 60 mM potassium chloride (6781.3, Carl Roth) and 2 mM sodium phosphate (T879.1 and 4984.2, Carl Roth) at pH 7.5. We include an oxygen scavenging system consisting of 1.2 mg/mL glucose (G7528, Merck), 0.04 mg/mL glucose oxidase (G6125-10KU, Merck), 0.008 mg/mL catalase (C9322-1G, Merck) and 20 mM DTT (6908.2, Carl Roth). Additional 0.01 mM taxol (T1912-1MG, Merck) stabilizes the microtubules. For measurements with TX100, we add 0.1 % (w/v) Triton-X 100 (TX100; 3051.3, Carl Roth) and in case of measurements with a total magnesium concentration of 20 mM, we add 18 mM $MgCl_2$. We filter the solutions with a cellulose acetate membrane filter with a pore size of 0.2 µm (7699822, Th. Geyer, Renningen, Germany).

## Optical trapping experiment

We perform the OT experiments using a commercial setup (C-Trap, LUMICKS, Amsterdam, The Netherlands) which is equipped with quadruple optical tweezers, a microfluidic chip and a confocal microscope. Beads, microtubules, measuring buffer and IFs are flushed into four

inlets to the microfluidic chip as sketched in Fig. 2a. For each measurement, four beads are captured and then calibrated in the buffer channel using the thermal noise spectrum (Fig. 2aI). One bead pair (beads 1 and 2) is moved to the vimentin IF channel and incubated there until a filament binds to beads (Fig. 2aII.). Meanwhile, the other bead pair (beads 3 and 4) is kept in the measuring buffer channel, so that no filaments adhere to those beads. To capture a microtubule (Fig. 2aIII.), beads 3 and 4 are moved to the microtubule channel, while bead 1 and 2 stay in the measuring buffer channel. Once a microtubule is bound to beads 3 and 4 and an IF to beads 1 and 2, the bead pair with the IF is horizontally turned by 90° (Supplementary Fig. 3a) and moved up in $z$-direction by 4.9 µm. The bead pair holding the IF is moved in the $x$-$y$-plane so that the central part of the IF is positioned above the center of the microtubule (Fig. 2aIV. and Supplementary Fig. 3a). To bring the IF and microtubule into contact, the IF is moved down in $z$-direction until the microtubule is pushed into focus or slightly out of focus. The IF is moved perpendicularly to the microtubule in the $x$-$y$-plane at 0.55 µm/s, while we measure the forces in the $x$- and $y$-direction on bead 1. Simultaneously, we record confocal images to see whether an interaction occurs. In case no interaction occurs after two movements in the $x$-$y$-plane, the IF is moved down in $z$-direction by 0.4 µm and the movement in the $x$-$y$-plane is repeated. The experiment ends when the microtubule breaks off the bead, or the IF or microtubule breaks. We measured 57 pairs of microtubules and vimentin IFs in CB, 38 pairs with TX100 and 36 pairs with additional magnesium chloride. In total, we moved the IFs 744 times perpendicularly to the microtubules in CB, 704 times in CB with TX100 and 542 times in CB with additional magnesium chloride.

The OT data are processed with self-written Matlab (MathWorks, Natick, Massachusetts, USA) scripts. For each filament pair, we analyze the component of the force $F_{1y}$ acting on bead 1 in the $y$-direction, since the forces in $x$-direction are balanced by the IF, as sketched in Supplementary Fig. 3b. From the raw force data, we manually select the force data containing an interaction. Due to interactions of the energy potentials of the different traps,

some data sets exhibit a linear offset which we subtract from the data. From the interaction-free force data, we determine the experimental error by calculating the standard deviation in the force of the first 20 data points. We define an interaction as soon as the force $F_{1y}$ as shown in Fig. 2d deviates by more than $5\sigma_F$ from the mean of the first 20 data points, where $\sigma_F$ is the standard deviation of the force without interactions in each data set. The force increases as shown for a typical measurement in Fig. 2d, until the interaction ends with a fast force decrease as marked by $\Delta F_{1y}$. We do not take breaking forces below 0.5 pN into account because they may be caused by force fluctuations. Since the force detection of trap 1 is the most accurate one in the setup, we analyze the force on bead 1 only. To determine the total breaking force $F_B$, we multiply the force $F_{1y}$ acting on bead 1 in $y$-direction with a correction factor $c_F$ that is based on the geometry of the experiment. $c_F$ depends on the distance between bead 1 and 2 $d_{\mathrm{MT}}$ and the distance $d_{\text{IF-MT}}$ from bead 1 to the contact point of the IF and the microtubule as sketched in Supplementary Fig. 3c:

$$c_F = \frac{d_{\mathrm{MT}}}{d_{\text{IF-MT}}} \,. \tag{3}$$

For the total force $F_C$ acting on the IF-microtubule bond, we get:

$$F_C = c_F F_{1y} \,.$$

Thus, when an IF-microtubule bond breaks, the total force difference $F_B$ is:

$$F_B = c_F \Delta F_{1y} \,. \tag{4}$$

## Preparation of passivated cover glasses for TIRF experiments

We clean cover glasses (26x76 mm$^2$, no. 1, Thermo Scientific) by successive chemical treatments: (i) We incubate the cover glasses for 30 min in acetone and then (ii) for 15 min in ethanol (96% denatured, 84836.360, VWR, Radnor, Pennsylvania, USA), (iii) rinse them

with ultrapure water, (iv) leave them for 2 h in Hellmanex III (2% (v/v) in water, Hellma Analytics, Müllheim, Germany), and (v) rinse them with ultrapure water. Subsequently, we dry the cover glasses using nitrogen gas flow and incubate them for three days in a 1 mg/mL solution of 1:10 silane-PEG-biotin (PJK-1919, Creative PEG Works, Chapel Hill, North Carolina, USA) and silane-PEG (30 kDa, PSB-2014, Creative PEG Works) in 96% ethanol and 0.02% v/v hydrochloric acid, with gentle agitation at room temperature. We subsequently wash the cover glasses in ethanol and ultrapure water, dry them with nitrogen gas and store them at 4°C for a maximum of four weeks.

## TIRF experiments

We use an inverted microscope (IX71, Olympus, Hamburg, Germany) in TIRF mode equipped with a 488-nm laser (06-MLD, 240 mW, COBOLT, Solna, Sweden), a 561-nm laser (06-DPL, 100 mW, COBOLT) and an oil immersion TIRF objective (NA = 1.45, 150X, Olympus). We observe microtubule dynamics by taking an image every 5 s for 15 – 45 min using the CellSense software (Olympus) and a digital CMOS camera (ORCA-Flash4.0, Hamamatsu Photonics, Hamamatsu, Japan).

For TIRF experiments, we build flow chambers from passivated cover glasses and double sided tape (70 µm height, 0000P70PC3003, LiMA, Couzeix, France). We flush 50 µg/mL neutravidin (A-2666, Invitrogen, Carlsbad, California, USA) in BRB80 into the chamber and incubate for 30 s. To remove free neutravidin, we wash with BRB80. Afterwards, we flush microtubule seeds diluted 300 x in BRB80 into the chamber and incubate for 1 min before we remove free floating seeds by washing with BRB80 supplemented with 1% BSA. Then, a mix containing 0.5 mg/mL (corresponding to 2.34 µM) vimentin tetramers (4% ATTO-565-labeled), 20 µM or 25 µM tubulin (20% ATTO488-labelled), 0.65% BSA, 0.09% methyl cellulose, 2 mM phosphate buffer, 2 mM $MgCl_2$, 25 mM PIPES, 1 mM EGTA, 60 mM KCl, 20 mM DTT, 1.2 mg/mL glucose, 8 µg/mL catalase and 40 µg/mL glucose oxidase, pH 7.5, is perfused into the chamber. To avoid evaporation and convective flow, we close

the chamber with vacuum grease and place it on the stage of the TIRF microscope that is kept at 37°C.

From the TIRF movies, kymographs are created using the reslice function of ImageJ (ImageJ V, version 2.0.0-rc-69/1.52p). From the kymographs, microtubule growth velocities, catastrophe and rescue frequencies are estimated. We calculate the catastrophe frequency for each experiment as

$$f_{\text{cat,exp}} = \frac{\text{total number of catastrophe events}}{\text{total microtubule growth time}}$$

and the rescue frequency as

$$f_{\text{resc}} = \frac{\text{total number of rescue events}}{\text{total microtubule depolymerization time}}$$

The total growth time is 800-2000 min per condition, the total depolymerization time 50-70 min per condition.

## Determination of vimentin filament length distributions

To measure the lengths of vimentin filaments (see Supplementary Fig. 1), we prepare five 1.5 mL reaction tubes with 15 µL of a mix of 2.3 µM vimentin tetramers in CB including all additions as used for the TIRF experiments such as methyl cellulose, GTP and oxygen scavenger (see previous section for the exact composition of the buffer). We then incubate the mix at 37°C for 5, 10, 20, 30 or 45 min. The filament assembly is stopped by adding 25 volumes of buffer to the tubes. 5 µL of each diluted mix are then pipetted on a cover glass and a second cover glass is placed on top. Images are taken with an inverted microscope (IX81, Olympus) using the CellSense software (Olympus), a 60x oil-immersion PlanApoN objective (Olympus) and an ORCA-Flash 4.0 camera (Hamamatsu Photonics). The filament lengths are measured using the semi-automated JFilament 2D plugin (Lehigh University, Bethlehem, PA, USA, version 1.02) for ImageJ (version 2.0.0-rc-69/1.52p).

# Modeling

## Parameters for optical trapping experiments and modeling

Table 1: Parameters obtained from OT experiments (E), from modeling (M) and from literature (L).

| Parameter | Description | Value | E/M/L |
|---|---|---|---|
| $b(t)$ | Probability that an IF-microtubule bond is closed | | E, M |
| $\Delta G_{\text{IF-MT}}$ | IF-microtubule bond energy in pure CB | $(2.3 \pm 1.3)\, k_B T$ | E, M |
| $\Delta G_{\text{IF-MT,TX100}}$ | IF-microtubule bond energy with additional TX100 | $(2.1 \pm 0.6)\, k_B T$ | E, M |
| $\Delta G_{\text{IF-MT,Mg}}$ | IF-microtubule bond energy with additional magnesium chloride | $(3.0 \pm 1.0)\, k_B T$ | E, M |
| $d_{\text{IF}}$ | Length of the filament between the IF-microtubule interaction junction and bead 3 in OT experiments as sketched in Supplementary Fig. 3c | | E |
| $E_{Ab}$ | Binding activation energy of an IF-microtubule bond | | M |
| $E_{Au}$ | Unbinding activation energy of an IF-microtubule bond | | M |
| $f(t)$ | Density function of the exponential distribution to determine the time (un-)bindung of an IF-microtubule bond | | M |
| $F_B$ | Breaking force in OT experiments | | E |

| | | | |
|---|---|---|---|
| $F_e$ | Force increase during entropic stretching of a vimentin IF | | M |
| $k_B$ | Boltzmann constant | $1.38 \cdot 10^{-23}$ J/K | L[64] |
| $\lambda$ | Mean time until an (un-)binding event of an IF-microtubule bond | | M |
| $L_C$ | Contour length of a vimentin IF | | E |
| $L_P$ | Persistence length of a vimentin IF | 1.5 µm | L[58,65] |
| $n_i$ | Total number of IF-microtubule interactions of OT experiments in a specific buffer | | E |
| $p_b(t)$ | Probability that a bond closes at a certain time $t$ | | M |
| $p_u(t)$ | Probability that a bond unbinds at a certain time $t$ | | M |
| $r_{b,0}$ | Constant prefactor of the binding rate $r_b(t)$ | | M |
| $r_{b,\mathrm{eff}}$ | Effective binding rate in pure CB | $1.07 \cdot 10^{-2}$ s$^{-1}$ | E |
| $r_{b,\mathrm{eff,TX100}}$ | Effective binding rate with additional TX100 | $0.56 \cdot 10^{-2}$ s$^{-1}$ | E |
| $r_{b,\mathrm{eff,Mg}}$ | Effective binding rate with additional magnesium chloride | $1.3 \cdot 10^{-2}$ s$^{-1}$ | E |
| $r_b(t)$ | Force-dependent binding rate of a vimentin IF and a microtubule | | M |
| $r_{u,0}$ | Constant prefactor of the unbinding rate $r_u(t)$ | | M |
| $r_{u,\mathrm{eff}}$ | Effective unbinding rate in pure CB | $(0.11 \pm 0.10)$ s$^{-1}$ | M |

| | | | |
|---|---|---|---|
| $r_{u,\mathrm{eff,TX100}}$ | Effective unbinding rate with additional TX100 | $(0.26 \pm 0.20)$ s$^{-1}$ | M |
| $r_{u,\mathrm{eff,Mg}}$ | Effective unbinding rate with additional magnesium chloride | $(0.15 \pm 0.08)$ s$^{-1}$ | M |
| $r_u(t)$ | Force-dependent unbinding rate of a microtubule and a vimentin IF | | M |
| $t$ | Time | | E, M |
| $t^*$ | Duration of entropic stretching of a vimentin IF in OT experiments | | M |
| $t_b$ | Time until binding of an IF-microtubule bond | | E, M |
| $t_{\mathrm{cont}}$ | Total time in which the IF and microtubule are unbound in OT experiments in a certain buffer | | E |
| $t_u$ | Duration of a closed IF-microtubule bond | | E, M |
| $\mathrm{d}t$ | Discretization time step | 0.05 s | M |
| $\tau$ | Time scale of force decrease in OT experiments | 0.1 s | E, M |
| $T$ | Temperature | | E, M |
| $v$ | Velocity of the lowest bead 3 as sketched in Supplementary Fig. 3 during OT experiments | 0.55 µm/s | E |
| $w$ | Final constant loading rate in OT experiments | | E |
| $x$ | End-to-end distance of a vimentin IF | | E, M |

| | | | |
|---|---|---|---|
| $x_u$ | Distance from bound to transition state in pure CB | $(0.17 \pm 0.05)$ nm | M |
| $x_{u,\mathrm{TX100}}$ | Distance from bound to transition state with additional TX100 | $(0.23 \pm 0.13)$ nm | M |
| $x_{u,\mathrm{Mg}}$ | Distance from bound to transition state with additional magnesium chloride | $(0.08 \pm 0.08)$ nm | M |

## Two-state model for IF-microtubule interactions

We model IF-microtubule interactions as single molecular bonds to understand the force-dependent behavior in different buffer conditions. The bond can either be in a closed or in an open state with force-dependent stochastic transitions between these two states, as sketched in Fig. 4b. In the experiment, we move the IF with a constant speed $v$ perpendicularly to the microtubule, as shown in Fig. 2b and Supplementary Fig. 3a. Once the bond closes, the IF with an average persistence length of $L_P = 1.5$ µm[58,65] is stretched to its full contour length $L_C$. Thus, the entropic force $F_e$ relates to the end-to-end distance $x = vt$ as[37,38]

$$\frac{x}{d_{\mathrm{IF}}} = \coth\left(\frac{2L_P F_e}{k_B T}\right) - \frac{k_B T}{2L_P F_e} \tag{5}$$

with the Boltzmann constant $k_B$ and the temperature $T$. $d_{\mathrm{IF}}$ is the length of the filament between the IF-microtubule junction and bead 3 as sketched in Supplementary Fig. 3c.

In the simulation, we assume a linear force increase from time $t^*$ on.[39,40] The linear force increase is set by the experimental force rate $w$, which we determine from a linear fit to the second half of the experimental force data of each interaction. $t^*$ is determined as the time when the force increase $\frac{dF_e}{dt}$ due to a decreasing entropy is the same as the experimental force rate $w$, i.e. $w = \frac{dF_e}{dt^*}$:

$$F(t) = \begin{cases} F_e(x = vt) & \text{for } \ t < t^* \\ wt & \text{for } t > t^* \end{cases} , \tag{6}$$

Once the bond breaks at a force $F_B$ after a time $t_u$, we assume an exponential force relaxation on a characteristic time scale of $\tau$:

$$F(t) = F_B \exp(-(t - t_u)/\tau) \text{ for } t > t_u. \tag{7}$$

We indeed observe a fast, exponential-like force decay in our experiments. However, the time resolution is not sufficient to fit $\tau$ precisely. We set $\tau = 0.1$ s as this results in force versus time curves similar to our experiments.

All variables with the index $b$ refer the binding process and the index $u$ represents the unbinding process. We describe the force-dependent binding and unbinding rates as follows: We assume that the binding and unbinding rates $r_b(t)$ and $r_u(t)$, respectively, depend on a reaction prefactor $r_{b,0/u,0}$, the activation energy for binding or unbinding $E_{Ab/Au}$, the thermal energy $k_BT$ and the potential width of the two states $x_{b/u}$:[41]

$$r_b(t) = r_{b,0} \exp\left(\frac{-E_{Ab}}{k_BT}\right) \cdot \exp\left(\frac{-F(t)x_b}{k_BT}\right) , r_u(t) = r_{u,0} \exp\left(\frac{-E_{Au}}{k_BT}\right) \cdot \exp\left(\frac{F(t)x_u}{k_BT}\right) . \tag{8}$$

The force-independent parameters $r_{b,0/u,0}$ and $E_{Ab/Au}$ result in an effective zero-force rate

$$r_{b,\text{eff}/u,\text{eff}} = r_{b,0/u,0} \exp\left(\frac{-E_{Ab/Au}}{k_BT}\right) ,$$

in which $r_{b,\text{eff}}$ can be determined from the experimental data in Fig. 3c, e and g: We calculate the total contact time $t_{\text{cont}}$ of the IF and microtubule without an interaction and the number of initiated interactions $n_i$ between IFs and microtubules from the experimental data:

$$r_{b,\text{eff}} = \frac{n_i}{t_{\text{cont}}} \, .$$

If we assume the same prefactor for the binding or unbinding process, i.e. $r_{b,0} = r_{u,0}$,[41] the ratio of two effective binding or unbinding rates for different experimental buffer conditions 1 and 2, or two different states (bound, unbound) sheds light on the differences in the activation energies for these buffer conditions or states. For the binding rates for two different buffer conditions, the activation energy difference is:

$$\frac{r_{b,\text{eff},1}}{r_{b,\text{eff},2}} = \frac{\exp\left(\frac{-E_{Ab,1}}{k_B T}\right)}{\exp\left(\frac{-E_{Ab,2}}{k_B T}\right)} \Rightarrow k_B T \ln\left(\frac{r_{b,\text{eff},1}}{r_{b,\text{eff},2}}\right) = E_{Ab,2} - E_{Ab,1} \, , \tag{9}$$

and likewise for the rates for the unbound state.

In the same way, we can calculate the absolute energy difference $\Delta G_{\text{IF-MT}}$ between the bound and unbound state for the same buffer condition:[41]

$$\Delta G_{\text{IF-MT}} = -k_B T \ln\left(\frac{r_{u,\text{eff}}}{r_{b,\text{eff}}}\right) \, . \tag{10}$$

Here, the sum of the potential widths $x_b + x_u$ nm provides the total distance between the bound and unbound state, which we assume to be the same for all experimental conditions. The rate equations in Eq. (8) ensure that detailed balance is satisfied.[41]

Thus, from these considerations and from the experiment, we know $L_C$, $w$, $\tau$ and $r_{b,\text{eff}}$, but neither $r_{u,\text{eff}}$ nor $x_b$ or $x_u$. We simulate the binding and unbinding reactions for the known parameters and vary $x_u$ from 0 nm up to 0.9 nm in steps of 0.01 nm and $r_{\text{eff},u}$ from 0.02 up to 0.6 $\text{s}^{-1}$ in steps of 0.01 $\text{s}^{-1}$. We determine $x_b$ by calculating $x_b = 0.4\,\text{nm} - x_u$, since the maximum value of $x_u$ is below 0.4 nm.

The binding and unbinding process cannot be described in a closed analytical expression due to the time dependence in the exponential expression of the reaction rates.[66] Therefore, we consider two different approaches to determine the breaking force histograms which we

compare to the experimental data: (i) We solve the rate equations directly numerically, which is the fastest way to calculate the force histograms. (ii) We simulate the force-time trajectories of single bonds, which allows us to directly compare single simulated trajectories to our experimental data. Both approaches result in the same force histograms as shown in Fig. 3c, e and g.

## Numerical solution of the two-state Model

To solve the rate equations in Eq. (8) numerically, we define $b(t)$ as the probability that the IF-microtubule bond is closed. Thus, the temporal behavior of $b$ can be described as:

$$\frac{\mathrm{d}b}{\mathrm{d}t} = -r_u(t) \cdot b(t) + r_b(t)(1 - b(t)) \,, \tag{11}$$

$$= -b(t) r_{u,\mathrm{eff}} \exp\left(\frac{F(t)x_u}{k_B T}\right) + (1 - b(t)) r_{b,\mathrm{eff}} \exp\left(\frac{-F(t)x_b}{k_B T}\right) \,. \tag{12}$$

We solve numerically for $b(t)$ with the Matlab function `ode45`. To obtain a histogram of breaking forces, we differentiate $b(t)$ with respect to $t$ and, thus, determine the probability $p_u(t)$ that the IF and microtubule unbind at a certain time $t$:

$$p_u(t) = -\frac{\mathrm{d}b}{\mathrm{d}t} \,.$$

To calculate the probability-force diagram, which we know from experiments, we determine $p_u$ as a function of $F$, i.e. $p_u(t(F))$ by inverting $F(t)$ as described in Eq. (6).

## Monte-Carlo simulation of single molecular bonds described by the two-state model

To obtain single force-time trajectories of an IF-microtubule bond, we simulate the binding and unbinding process in several steps: (i) The time until an individual binding event is

determined by choosing a random time $t_b$ from an exponential distribution with the density function $f(t)$ and a mean value of $\lambda = (r_b(t, F = 0))^{-1}$:[67,68]

$$f(t) = \lambda \exp(-\lambda t)\,.$$

The bond is now closed after time $t_b$. The force starts to increase as described in Eq. (6). (ii) As the unbinding rate depends on the force, which increases with time, the mean $(r_u(F(t)))^{-1}$ of the exponentially distributed unbinding time $t_u$ changes with increasing force. Thus, it is not straightforward to determine the time until unbinding with a single step as in (i). Instead, we split $t_u$ into small time intervals $\mathrm{d}t$. We set $\mathrm{d}t = 0.05$ s as a compromise between accuracy and computation time, which is the same as the experimental time resolution. The time is increased in steps of $\mathrm{d}t$ and after each step, the unbinding rate is evaluated. The probability $p_u$ that the bond breaks in the considered time interval is $p_u = r_u(F(t))\mathrm{d}t$, where we approximate the exponentially increasing unbinding rate as a constant for small $\mathrm{d}t$. If a random number drawn from a uniform distribution between 0 and 1 is greater than $p_u$, the bond stays closed, otherwise it opens. If the bond remains closed, the time is increased by $\mathrm{d}t$, the force is updated and step (ii) is repeated until the bond breaks. (iii) Once the bond breaks, the force decreases as described by Eq. (7). Since the bond can close with a force-dependent rate while the force decays, the time is increased stepwise again and the probability to rebind is evaluated as in step (ii) with $p_b = r_b(t, F(t))\mathrm{d}t$. If the force decreases to a value below 0.001 pN, the force is set to 0 pN and the algorithm is repeated starting at step (i).

As the IFs and microtubules have slightly different lengths for different measurements, the force rate differs between the experiments. To account for these different rates, we run the simulation until 1000 breaking events are recorded for each experimental force rate $w$. The final distribution of breaking forces results from the normalized sum of distributions of breaking forces for all force rates. This final distribution is compared to the experimental data

with the Kolmogorov-Smirnov test.[69] If the experimental and the simulated distributions do not differ more than allowed for a 5% significance level,[69] we accept the parameters $r_{u,\mathrm{eff}}$ and $x_u$ as shown in Fig. 4a. To calculate the energy diagram in Fig. 4b, we determine the centroids of the accepted parameter regions in Fig. 4a. We determine the standard deviations from the distributions in Fig. 4a assuming that $r_{u,\mathrm{eff}}$ and $x_u$ are independent. The simulated breaking force histograms do not depend on the exact value of $x_b$ in the range of 0.2 to 1.5 nm since $r_{b,\mathrm{eff}}$ dominates the force-dependent term in Eq. (1). We do not observe a sufficient number of rebinding events under force to determine $x_b$ from the experiment. For clarity, $x_b + x_u$ is set to 0.4 nm in Fig. 4.

## Parameters for TIRF experiments, modeling and simulations

Table 2: Parameters obtained from OT experiments (O), from TIRF experiments (T), from modeling of TIRF experiments (M), simulation input parameters (I) and parameters known from literature (L).

| Parameter | Description | Value | O/T/M/I/L |
|---|---|---|---|
| $a_{\mathrm{IF}}$ | Diameter of a vimentin IF | 11 nm | L[60] |
| $d$ | Dimensions in which a vimentin filament can diffuse during TIRF experiments | 3 | M |
| $D$ | Average diffusion coefficient of a vimentin filament in the TIRF experiment | | L,[70] M |
| $\Delta G_{\mathrm{IF\text{-}MT}}$ | Association energy of a vimentin IF to a microtubule | $(2.3 \pm 1.3)\ k_B T$ | O |
| $\Delta G_{\mathrm{latd}}$ | Lateral association energy of a GDP dimer | $1.5\ k_B T$ | I |

| | | | |
|---|---|---|---|
| $\Delta G_{\text{latt}}$ | Lateral association energy of a GTP dimer | 3.5 $k_B T$ | I |
| $\Delta G_{tb}$ | Total average energy of a tubulin dimer in the microtubule lattice before catastrophe | 5.1 $k_B T$ (20 µM), 5.2 $k_B T$ (25 µM) | O, T, M |
| $f_{\text{cat, exp}}$ | Experimentally observed catastrophe frequency of microtubules with surrounding vimentin IFs | 0.123 $\text{min}^{-1}$ (20 µM), 0.107 $\text{min}^{-1}$ (25 µM) | T |
| $f_{\text{cat, IF-MT}}$ | Catastrophe frequency of microtubules while interacting with a vimentin IF | | M |
| $f_{\text{cat, MT}}$ | Experimentally observed catastrophe frequency of microtubules | 0.180 $\text{min}^{-1}$ (20 µM), 0.156 $\text{min}^{-1}$ (25 µM) | T |
| $f_{\text{resc}}$ | Simulation rescue frequency at 25 µM tubulin without IFs | 0.03 $\text{s}^{-1}$ | I |
| $f_{\text{resc, IF}}$ | Simulation rescue frequency at 25 µM tubulin with IFs | 0.17 $\text{s}^{-1}$ | I |
| $\zeta$ | Mesh size of the vimentin network in TIRF experiments | 0.63 µm | E, L[32,71] |
| $\eta$ | Viscosity of sample studied in TIRF experiments | 3 mPas | L[72] |
| $l_m$ | length of a vimentin IF monomer when incorporated in a filament | 42 nm | L[60] |
| $L_P$ | Persistence length of a vimentin IF | 1.5 µm | L[58,65] |
| $n$ | Number of lateral neighbors of a tubulin dimer | | I |

| | | | |
|---|---|---|---|
| $n_{\mathrm{IF}}$ | Number of monomers of a vimentin IF which may interact with a microtubule when the IF and microtubule are in contact | | M |
| $n_{\mathrm{MT}}$ | Number tubulin dimers which may interact with a vimentin monomer when the IF and microtubule are in contact | | M |
| $n_{\mathrm{pf}}$ | Number of protofilaments in a simulated microtubule | 13 | L[73] |
| $p_{bV}$ | Percentage of time a vimentin filament spends at the bottom of a certain volume | 4% | M |
| $p_{\mathrm{geo}}$ | Probability that a vimentin monomer is in contact with a tubulin dimer during a TIRF experiment | 10.5% | M |
| $p_i$ | Probability that a vimentin monomer interacts with a tubulin dimer | 40% | O, T, M |
| $r$ | Random number between 0 and 1 | | I |
| $r_{b,md}$ | Binding rate per vimentin monomer and tubulin dimer | | M |
| $r_c$ | Collision rate of a vimentin monomer and a tubulin dimer | $15\ \mathrm{s}^{-1}$ | M |
| $r_{dd,0}$ | Depolymerization rate of a GDP dimer without lateral neighbors | $643\ \mathrm{s}^{-1}$ | I |
| $r_{dt,0}$ | Depolymerization rate of a GTP dimer without lateral neighbors | $9.93 \cdot 10^{-4}\ \mathrm{s}^{-1}$ | I |

| | | | |
|---|---|---|---|
| $r_{dd}$ | Depolymerization rate of a GDP dimer taking the number of neighbor dimers into account | | I |
| $r_{dt}$ | Depolymerization rate of a GTP dimer taking the number of neighbor dimers into account | | I |
| $r_{hy}$ | Hydrolysis rate of GTP dimers | 7 $s^{-1}$ | I |
| $r_i$ | Interaction rate of IFs and microtubules in the TIRF experiments | 0.07 $s^{-1}$ | M |
| $r_{g,20}$ | Polymerization rate of GTP dimers per protofilament for 20 µM free tubulin concentration | 1.3 $s^{-1}$ | I |
| $r_{g,25}$ | Polymerization rate of GTP dimers per protofilament for 25 µM free tubulin concentration | 2.2 $s^{-1}$ | I |
| R | Any reaction rate in simulation | | I |
| $t$ | Time | | M |
| $\tau_d$ | Time it takes a filament to diffuse through a certain volume | | M, L[74] |
| $v_d$ | Approximate velocity of a diffusing vimentin IF in a certain volume | | M |
| $z$ | Random number between 0 and 1 | | I |

## Model of a dynamic microtubule

We base our model of a dynamic microtubule on Refs. 20 and 26 and run Monte-Carlo simulations with a self-written Python code (Beaverton, Oregon, USA) to obtain simulated kymographs. We assume a microtubule lattice with $n_{\mathrm{pf}} = 13$ protofilaments that has a

helical pitch of 3 monomers per turn as sketched in Fig. 5a. Thus, there is a seam formed by protofilaments 1 and 13, which are displaced by 1.5 dimers. All dimers incorporated in the lattice interact with two lateral and two longitudinal dimer positions. At the seam, the dimers interact with two half dimers across the seam. The microtubule is represented by a matrix in the simulation and the state of the dimer is entered at a corresponding position in the matrix. A dimer position can be either unoccupied or occupied by a GTP dimer (purple in Fig. 5a, b), a GDP dimer (blue in Fig. 5a, b) or a GMPCPP-dimer (green in Fig. 5a, b). We set the first three dimer layers to GMPCPP dimers, which represent the seed in the experiment. The GMPCPP dimers cannot depolymerize. To avoid artifacts from the starting conditions, we start the simulations with a microtubule consisting of 30 layers of GDP dimers, which have four layers of GTP dimers on top representing the tip.[20]

To simulate microtubule dynamics, we determine four different reaction rates (i–iv) as sketched in Fig. 5a (top): (i) The polymerization rate $r_g$ when a GTP dimer binds to the tip of the microtubule, (ii) the depolymerization rate $r_{dt}$ of a GTP dimer when a GTP dimer falls off the lattice, (iii) the hydrolysis rate $r_{hy}$ of a GTP dimer to a GDP dimer and (iv) the depolymerization rate $r_{dd}$ of GDP dimers. Since we use a buffer which is also compatible with vimentin filament assembly, these simulation parameters differ from the parameters used in literature.[20,27,75] We summarize all important simulation parameters in Table 2. We calculate the different reaction rates (i–iv) as follows:

(i) The polymerization rate for GTP dimers is concentration dependent.[20] To match the growth rate to the experimentally observed one, we set it to $r_{g,20} = 1.3$ dimers s$^{-1}$ per protofilament for 20 µM free tubulin concentration and to $r_{g,25} = 2.2$ dimers s$^{-1}$ per protofilament for 25 µM free tubulin concentration.

(ii)/(iv) The depolymerization rate of GTP and GDP dimers depends on the number of lateral neighbors $n$. For each lateral dimer, the depolymerization rate is lowered by a factor of $\exp(-\Delta G_{\mathrm{latt/latd}})$ due to the change in total bond energy $\Delta G_{\mathrm{latt}} = 3.5\ k_B T$ for a GTP dimer and $\Delta G_{\mathrm{latd}} = 1.5\ k_B T$ for a GDP dimer:[20]

$$r_{dt/dd} = r_{dt/dd,0} \exp\left(\frac{-n\Delta G_{\text{latt/latd}}}{k_B T}\right) , \tag{13}$$

For no lateral dimers, we assume an unbinding rate of $r_{dt,0} = 9.93 \cdot 10^{-4}$ s$^{-1}$ for GTP and $r_{dd,0} = 643$ s$^{-1}$ for GDP. We assume that only the dimers at the tip of a protofilament can depolymerize.[26]

(iii) We set the hydrolysis rate to 7 s$^{-1}$ to obtain a tip size which results in the same change in catastrophe frequency as observed in our experiments. This rate is on the same order of magnitude as assumed in Ref. 20. A dimer can only hydrolyze, if it has a neighbor in the same protofilament towards the direction of growth.[20,26] Since we do not observe rescue in our experiments for a free tubulin concentration of 20 µM and the precise reason for rescue is unknown,[75] we assume that the rapidly disassembling microtuble is "locked" in the disassembly state and no rescue occurs because GTP dimers polymerize faster then GDP dimers depolymerize.[75] Yet, we observe rescue at a concentration of 25 µM, which we implement in our simulation as occurring with a rate of $f_{\text{resc}} = 0.03$ s$^{-1}$.[75]

To simulate a kymograph of a dynamic microtubule, we calculate all possible reaction rates. For each possible reaction with rate $R$, a random number $z$ between 0 and 1 is drawn, with which we determine the time until the next realization of a certain reaction:[20,67]

$$t = \frac{-\ln z}{R} . \tag{14}$$

The reaction with the smallest time is set to be the next occurring reaction. The microtubule matrix containing the dimer states is updated correspondingly as shown for a snapshot of a typical microtubule configuration in Fig. 5b. We run 100 simulations for a total simulated time of 900 s each to obtain comparable amounts of experimental and simulated data. We record the length of the shortest protofilament during the simulation, which results in simulated kymographs. We plot typical simulated kymographs in Fig. 5c (left) for 20 µM free tubulin without surrounding vimentin and in Fig. 5c (right) for 25 µM free

tubulin with surrounding vimentin.

## Model of a dynamic microtubule stabilized by IFs

Our OT experiments show that IFs directly interact with microtubules. By comparing the binding and unbinding rates, we determine the energy difference $\Delta G_{\text{IF-MT}}$ between the bound and unbound state of the IF-microtubule interactions. Thus, if an IF binds to a microtubule dimer, the total binding energy of the dimer in the microtubule lattice is increased by $\Delta G_{\text{IF-MT}}$, which lowers the total energy sum in the exponential term of Eq. (13):

$$r_{dt/dd} = r_{dt,0/dd,0} \exp\left(\frac{-n\Delta G_{\text{latt/latd}} - \Delta G_{\text{IF-MT}}}{k_B T}\right) . \tag{15}$$

From the OT experiments, we know the binding rate of IFs and microtubules. To estimate the collision rate of IFs and microtubules in the TIRF experiment, we determine the binding rate for one vimentin monomer and one tubulin dimer $r_{b,md}$ from $r_{b,\text{eff}}$. To do so, we normalize the binding rate $r_{b,\text{eff}}$ by the number of possibly interacting vimentin monomers $n_{\text{IF}}$ and tubulin dimers $n_{\text{MT}}$:

$$r_{b,md} = \frac{r_{b,\text{eff}}}{n_{\text{IF}} n_{\text{MT}} \frac{v}{l_m}} ,$$

where $v$ is the velocity of the IF moving perpendicular to the microtubule and $l_m$ is the length of a vimentin IF monomer incorporated in the filament. $v/l_m$ is the rate of $n_{\text{IF}}$ vimentin monomers which may interact with the microtubule during this movement. Note that $r_{b,md}$ is unitless and can also be understood as the probability of a vimentin monomer and a tubulin dimer to interact.

We calculate the average diffusive velocity $v_d$ of a vimentin filament in the TIRF experiment by determining the mesh size $\zeta = 0.63\,\mu\text{m}$ from the protein concentration of the vimentin network[71] and the time $\tau_d$ it takes for a filament to diffuse through a volume of $\zeta^3$. The estimated viscosity[76] $\eta \approx 3$ mPas of the sample in TIRF experiments deviates from the

viscosity of water, since the sample in TIRF experiments contains 0.09% methylcellulose. The diameter[77] $a_{\mathrm{IF}}$ of a vimentin filament is 11 nm. The diffusion occurs in three dimensions $d = 3$ with a diffusion coefficient[70] of $D = k_B T \ln(\zeta/a_{\mathrm{IF}})/(3\pi\zeta\eta)$. We determine the approximate diffusive velocity:

$$v_d = \frac{\zeta}{\tau_d} = \frac{\zeta 2dD}{\zeta^2} = \frac{2dk_B T \ln(\zeta/a_{\mathrm{IF}})}{\zeta^2 3\pi\eta} \,.$$

Since the vimentin filaments form a network and not all tubulin dimers are in touch with a filament at the same time, we calculate the geometric probability $p_{\mathrm{geo}}$ of a dimer to be in contact with an IF $p_{\mathrm{geo}} = 6a_{\mathrm{IF}}/\zeta = 0.105$. A vimentin filament can only interact with a microtubule with a diameter of $d_{MT} \approx 25$ nm, see Ref. 73, at the bottom of the sample, so that only $p_{bV} = d_{MT}/\zeta = 0.04$ of the total volume are relevant for interactions. Together with the binding rate $r_{b,md}$ from the OT experiments, we obtain an interaction rate $r_i$ of IFs and microtubules in the TIRF experiments:

$$\begin{aligned} r_i &= r_{b,md} n_{\mathrm{IF}} n_{\mathrm{MT}} \frac{v_d}{l_m} p_{\mathrm{geo}} p_{bV} \\ &= \frac{r_{b,\mathrm{eff}}}{n_{\mathrm{IF}} n_{\mathrm{MT}} \frac{v}{l_m}} \cdot n_{\mathrm{IF}} n_{\mathrm{MT}} \frac{v_d}{l_m} p_{\mathrm{geo}} p_{bV} \\ &= \frac{r_{b,\mathrm{eff}}}{v} v_d p_{\mathrm{geo}} p_{bV} \approx 0.07\,\mathrm{s}^{-1} \,. \end{aligned}$$

We calculate the probability $p_i$ that an IF is bound to a microtubule by assuming an equilibrium between binding and unbinding IFs:

$$r_i(1 - p_i) = r_{u,\mathrm{eff}} p_i \,.$$

The unbinding rate is determined from OT experiments as well. We find $p_i \approx 40\%$. Consequently, in our simulation, we draw a random number $r$ between 0 and 1 and if $r < p_i$, the depolymerization rate changes as described in Eq. (15). If $r > p_i$, the depolymerization

rate remains unchanged.

The additional binding energy of IFs to microtubules also decreases the depolymerization rate of potential rescue sites, thus, rescue occurs more often. Thus, the frequency for rescue sites with surrounding vimentin filaments increases from $f_{\text{resc}} = 0.03\ \text{s}^{-1}$ to $f_{\text{resc, IF}} = 0.17\ \text{s}^{-1}$. The rescue frequency of microtubules with surrounding filaments is lower than we would expect if we calculate $f_{\text{resc}} \exp(\Delta G_{\text{IF-MT}}/k_B T)\ \text{s}^{-1} = 0.3\ \text{s}^{-1}$, however, in the same order of magnitude. Our model is probably too simple to describe this discrepancy arising from the poorly understood rescue process.[75]

We do not observe binding of the IFs to tubulin dimers as Fig. 1b suggests, thus, the term for the growth rate remains unchanged.

## Estimate of tubulin dimer binding energy by combining results from optical trapping and TIRF experiments

We can estimate the tubulin dimer binding energy by combining the results from OT and TIRF experiments. First, we calculate the catastrophe frequency $f_{\text{cat, IF-MT}}$ of a microtubule when a vimentin filament continuously interacts with all dimers. We know the experimentally observed catastrophe frequency without vimentin in solution $f_{\text{cat,MT}}$ and with vimentin in solution $f_{\text{cat,exp}}$ from the TIRF experiments. The observed catastrophe frequency in presence of vimentin results from a combination of microtubules which are in contact with a vimentin IF and which are not in contact with an IF. The probability that a microtubule monomer and a vimentin IF are in contact is $p_i$. Thus, the observed catastrophe rate $f_{\text{cat,exp}}$ in presence of vimentin IFs and the catastrophe rate $f_{\text{cat, IF-MT}}$ for microtubules continuously interacting with a vimentin IF are:

$$f_{\text{cat,exp}} = (1-p_i) f_{\text{cat, MT}} + p_i f_{\text{cat, IF-MT}}$$
$$f_{\text{cat, IF-MT}} = \frac{f_{\text{cat,exp}} - (1-p_i) f_{\text{cat, MT}}}{p_i} \approx 0.039\,\text{min}^{-1} \text{ for 20 µM and } 0.035 \text{ min}^{-1} \text{ for 25 µM.}$$

During depolymerization of the microtubule, the additional energy of a GTP dimer in the microtubule lattice $\Delta G_{tb}$ is released. Therefore, we assume that the only energy difference between the dimer, which is incorporated in an microtubule and which unbinds from an IF monomer in the OT experiments, and the last dimer, which depolymerizes just before an microtubule catastrophe in the TIRF experiments, is $\Delta G_{tb}$. Thus, we can combine the catastrophe rates from TIRF experiments and the unbinding rates of the OT experiments to calculate $\Delta G_{tb}$:

$$\frac{r_{u,\text{eff}}}{f_{\text{cat,IF-MT}}} = \exp\left(\frac{\Delta G_{tb}}{k_B T}\right), \tag{16}$$
$$\Delta G_{tb} = k_B T \ln\left(\frac{r_{u,\text{eff}}}{f_{\text{cat,IF-MT}}}\right) \approx 5.1\, k_B T \text{ for } 20\,\text{µM and } 5.2\, k_B T \text{ for } 25\,\text{µM.}$$

# Acknowledgement

We thank Thomas Wenninger, Helge Schmidt and Sarah Adio for their support concerning the construction of the TIRF setup. We are grateful for purified tubulin and vimentin from Manuel Théry, Laurent Blanchoin, Jérémie Gaillard, Susanne Bauch. The work was financially supported by the European Research Council (ERC, Grant No. CoG 724932, to S.Kö.), the European Molecular Biology Organization (Long Term Fellowship No. 1164-2018, to L.S.) and the Studienstiftung des deutschen Volkes e.V. (fellowship to C.L.) This research was conducted within the Max Planck School Matter to Life (to S.Kö. and S. Kl.) supported by the German Federal Ministry of Education and Research (BMBF) in

collaboration with the Max Planck Society. The work further received financial support via an Excellence Fellowship of the International Max Planck Research School for Physics of Biological and Complex Systems (IMPRS PBCS, fellowship to A.V.S.).

## Author Contributions

S.Kö. conceived and supervised the project. S.Kö. and L.S. designed the experiments. L.S. and C.L. performed all experiments and analyzed the data. A.V.S. helped performing the quadruple optical trap experiments. C.L. and S.Kl. designed and performed numerical simulations. All authors contributed to writing the manuscript.

## Competing interests

The authors declare no competing interests.

## Data availability

The data that support the findings of this study are available from the corresponding authors upon reasonable request.

## Code availability

The source codes of the numerical simulations are part of the Supplementary Information. The codes for the analysis of the model simulations are available from the corresponding authors upon request.

# References


(1) Svitkina, T. M.; Verkhovsky, A. B.; Borisy, G. G. Plectin sidearms mediate interaction of intermediate filaments with microtubules and other components of the cytoskeleton. *J. Cell Biol.* **1996**, *135*, 991–1007.

(2) Chang, L.; Goldman, R. D. Intermediate filaments mediate cytoskeletal crosstalk. *Nat. Rev. Mol. Cell Biol.* **2004**, *5*, 601–613.

(3) Kim, H.; Nakamura, F.; Lee, W.; Hong, C.; Perez-Sala, D.; McCulloch, C. A. Regulation of cell adhesion to collagen via $\beta 1$ integrins is dependent on interactions of filamin A with vimentin and protein kinase C epsilon. *Exp. Cell Res.* **2010**, *316*, 1829–1844.

(4) Leube, R. E.; Moch, M.; Windoffer, R. Intermediate filaments and the regulation of focal adhesions. *Curr. Opin. Cell Biol.* **2015**, *32*, 13–20.

(5) Duarte, S.; Viedma-Poyatos, Á.; Navarro-Carrasco, E.; Martínez, A. E.; Pajares, M. A.; Pérez-Sala, D. Vimentin filaments interact with the actin cortex in mitosis allowing normal cell division. *Nat. Comm.* **2019**, *10*, 4200–4200.

(6) Serres, M. P.; Samwer, M.; Truong Quang, B. A.; Lavoie, G.; Perera, U.; Görlich, D.; Charras, G.; Petronczki, M.; Roux, P. P.; Paluch, E. K. F-Actin interactome reveals vimentin as a key regulator of actin organization and cell mechanics in mitosis. *Dev. Cell* **2020**, *52*, 210–222.e7.

(7) Goldman, R. D. The role of three cytoplasmic fibers in BHK-21 cell motility. I. Microtubules and the effects of colchicine. *J. Cell Biol.* **1971**, *51*, 752–762.

(8) Gyoeva, F. K.; Gelfand, V. I. Coalignment of vimentin intermediate filaments with microtubules depends on kinesin. *Nature* **1991**, *353*, 445–448.

(9) Gurland, G.; Gundersen, G. G. Stable, detyrosinated microtubules function to localize vimentin intermediate filaments in fibroblasts. *J. Cell Biol.* **1995**, *131*, 1275–1290.

(10) Yang, Y.; Dowling, J.; Yu, Q.-C.; Kouklis, P.; Cleveland, D. W.; Fuchs, E. An essential cytoskeletal linker protein connecting actin microfilaments to intermediate filaments. *Cell* **1996**, *86*, 655–665.

(11) Liao, G.; Gundersen, G. G. Kinesin is a candidate for cross-bridging microtubules and intermediate filaments. *J. Biol. Chem.* **1998**, *273*, 9797–9803.

(12) Leung, C. L.; Sun, D.; Zheng, M.; Knowles, D. R.; Liem, R. K. Microtubule actin cross-linking factor (MACF): A hybrid of dystonin and dystrophin that can interact with the actin and microtubule cytoskeletons. *J. Cell Biol.* **1999**, *147*, 1275–1285.

(13) Helfand, B. T.; Mikami, A.; Vallee, R. B.; Goldman, R. D. A requirement for cytoplasmic dynein and dynactin in intermediate filament network assembly and organization. *Mol. Biol. Cell* **2002**, *157*, 795–806.

(14) Bocquet, A.; Berges, R.; Frank, R.; Robert, P.; Peterson, A. C.; Eyer, J. Neurofilaments bind tubulin and modulate its polymerization. *J. Neurosci.* **2009**, *29*, 11043–11054.

(15) Uchida, A.; Alami, N. H.; Brown, A. Tight functional coupling of kinesin-1A and dynein motors in the bidirectional transport of neurofilaments. *Mol. Biol. Cell* **2009**, *20*, 4997–5006.

(16) Sakamoto, Y.; Boeda, B.; Etienne-Manneville, S. APC binds intermediate filaments and is required for their reorganization during cell migration. *J. Cell Biol.* **2013**, *200*, 249–258.

(17) Pallavicini, C.; Levi, V.; Wetzler, D. E.; Angiolini, J. F.; Benseñor, L.; Despósito, M. A.; Bruno, L. Lateral motion and bending of microtubules studied with a new single-filament tracking routine in living cells. *Biophys. J.* **2014**, *106*, 2625–2635.

(18) Gan, Z.; Ding, L.; Burckhardt, C. J.; Lowery, J.; Zaritsky, A.; Sitterley, K.; Mota, A.; Costigliola, N.; Starker, C. G.; Voytas, D. F.; Tytell, J.; Goldman, R. D.; Danuser, G.

Vimentin intermediate filaments template microtubule networks to enhance persistence in cell polarity and directed migration. *Cell Syst.* **2016**, *3*, 252–263.

(19) Colin, A.; Singaravelu, P.; Théry, M.; Blanchoin, L.; Gueroui, Z. Actin-network architecture regulates microtubule dynamics. *Curr. Biol.* **2018**, *28*, 2647–2656.

(20) VanBuren, V.; Odde, D. J.; Cassimeris, L. Estimates of lateral and longitudinal bond energies within the microtubule lattice. *Proc. Natl. Acad. Sci.* **2002**, *99*, 6035–6040.

(21) Castle, B. T.; Odde, D. J. Brownian dynamics of subunit addition-loss kinetics and thermodynamics in linear polymer self-assembly. *Biophys. J.* **2013**, *105*, 2528–2540.

(22) Kononova, O.; Kholodov, Y.; Theisen, K. E.; Marx, K. A.; Dima, R. I.; Ataullakhanov, F. I.; Grishchuk, E. L.; Barsegov, V. Tubulin bond energies and microtubule biomechanics determined from nanoindentation in silico. *J. Am. Chem. Soc.* **2014**, *136*, 17036–17045.

(23) Brouhard, G. J.; Rice, L. M. Microtubule dynamics: an interplay of biochemistry and mechanics. *Nat. Rev. Mol. Cell Biol.* **2018**, *19*, 451–463.

(24) Ganser, C.; Uchihashi, T. Microtubule self-healing and defect creation investigated by in-line force measurements during high-speed atomic force microscopy imaging. *Nanoscale* **2019**, *11*, 125–135.

(25) Kim, T.; Rice, L. M. Long-range, through-lattice coupling improves predictions of microtubule catastrophe. *Mol. Biol. Cell* **2019**, *30*, 1451–1462, PMID: 30943103.

(26) Schaedel, L.; Triclin, S.; Chrétien, D.; Abrieu, A.; Aumeier, C.; Gaillard, J.; Blanchoin, L.; Théry, M.; John, K. Lattice defects induce microtubule self-renewal. *Nat. Phys.* **2019**, *15*, 830–838.

(27) Hemmat, M.; Odde, D. J. Atomistic basis of microtubule dynamic instability assessed via multiscale modeling. Preprint at https://www.biorxiv.org/content/10.1101/2020.01.07.897439v1 (2020).

(28) Mitchison, T.; Kirschner, M. Dynamic instability of microtubule growth. *Nature* **1984**, *312*, 237–242.

(29) Walker, R. A.; O'Brien, E. T.; Pryer, N. K.; Soboeiro, F.; Voter, W. A.; Erickson, H. P.; Salmon, E. D. Dynamic instability of individual microtubules analyzed by video light microscopy: Rate constants and transition frequencies. *J. Cell Biol.* **1988**, *107*, 1437–1448.

(30) Vleugel, M.; Kok, M.; Dogterom, M. Understanding force-generating microtubule systems through in vitro reconstitution. *Cell Adh. Migr.* **2016**, *10*, 475–494.

(31) Blehm, B. H.; Schroer, T. A.; Trybus, K. M.; Chemla, Y. R.; Selvin, P. R. In vivo optical trapping indicates kinesin's stall force is reduced by dynein during intracellular transport. *Proc. Natl. Acad. Sci.* **2013**, *110*, 3381–3386.

(32) Pawelzyk, P.; Mücke, N.; Herrmann, H.; Willenbacher, N. Attractive interactions among intermediate filaments determine network mechanics in vitro. *Plos One* **2014**, *9*, e93194.

(33) Nogales, E.; Downing, K. H.; Amos, L. A.; Loewe, J. Tubulin and FtsZ form a distinct family of GTPases. *Nat. Struct. Biol.* **1998**, *5*, 451–458.

(34) Kadavath, H.; Hofele, R. V.; Biernat, J.; Kumar, S.; Tepper, K.; Urlaub, H.; Mandelkow, E.; Zweckstetter, M. Tau stabilizes microtubules by binding at the interface between tubulin heterodimers. *Proc. Natl. Acad. Sci.* **2015**, *112*, 7501–7506.

(35) Grosberg, A. Y.; Nguyen, T. T.; Shklovskii, B. I. The physics of charge inversion in chemical and biological systems. *Rev. Mod. Phys.* **2002**, *74*, 329–345.

(36) Shklovskii, B. I. Screening of a macroion by multivalent ions: Correlation induced inversion of charge. *Phys. Rev. E* **1999**, *60*, 5802–5811.

(37) Kuhn, W.; Grün, F. Beziehungen zwischen elastischen Konstanten und Dehnungsdoppelbrechung hochelastischer Stoffe. *Kolloid-Zeitschrift* **1942**, *101*, 248–271.

(38) James, H. M.; Guth, E. Theory of the Elastic Properties of Rubber. *J. Chem. Phys.* **1943**, *11*, 455–481.

(39) Lo, Y.-S.; Zhu, Y.-J.; Beebe, T. P. Loading-Rate dependence of individual ligand-receptor bond-rupture forces studied by atomic force microscopy. *Langmuir* **2001**, *17*, 3741–3748.

(40) Pohl, A.; Berger, F.; Sullan, R. M. A.; Valverde-Tercedor, C.; Freindl, K.; Spiridis, N.; Lefèvre, C. T.; Menguy, N.; Klumpp, S.; Blank, K. G.; Faivre, D. Decoding biomineralization: interaction of a Mad10-derived peptide with magnetite thin films. *Nano Lett.* **2019**, *19*, 8207–8215, PMID: 31565946.

(41) Kolomeisky, A. *Motor Proteins and Molecular Motors*; CRC press, Boca Raton, 2015.

(42) Meyers, R. A. *Encyclopedia of Molecular Cell Biology and Molecular Medicine*; Wiley VCH, New York, 2005.

(43) Romani, A. M. P. Cellular magnesium homeostasis. *Arch. Biochem. Biophys.* **2014**, *512*, 1–23.

(44) Lin, Y.-C.; Broedersz, C. P.; Rowat, A. C.; Wedig, T.; Herrmann, H.; MacKintosh, F. C.; Weitz, D. A. Divalent cations crosslink vimentin intermediate filament tail domains to regulate network mechanics. *J. Mol. Biol.* **2010**, *399*, 637–644.

(45) Dammann, C.; Nöding, B.; Köster, S. Vimentin networks at tunable ion-concentration in microfluidic drops. *Biomicrofluidics* **2012**, *6*, 022009.

(46) Dammann, C.; Köster, S. Dynamics of counterion-induced attraction between vimentin filaments followed in microfluidic drops. *Lab Chip* **2014**, *14*, 2681–2687.

(47) Janmey, P. A.; Slochower, D. R.; Wang, Y.-H.; Wen, Q.; Cebers, A. Polyelectrolyte properties of filamentous biopolymers and their consequences in biological fluids. *Soft Matter* **2014**, *10*, 1439–1449.

(48) Dammann, C.; Herrmann, H.; Köster, S. Competitive counterion binding regulates the aggregation onset of vimentin intermediate filaments. *Isr. J. Chem.* **2016**, *56*, 614–621.

(49) Rodriguez, O. C.; Schaefer, A. W.; Mandato, C. A.; Forscher, P.; Bement, W. M.; Waterman-Storer, C. M. Conserved microtubule-actin interactions in cell movement and morphogenesis. *Nat. Cell Biol.* **2003**, *5*, 599–609.

(50) Chung, B.-M.; Rotty, J. D.; Coulombe, P. A. Networking galore: intermediate filaments and cell migration. *Curr. Opin. Cell Biol.* **2013**, *25*, 600–612.

(51) Eckes, B.; Dogic, D.; Colucci-Guyon, E.; Wang, N.; Maniotis, A.; Ingber, D.; Merckling, A.; Langa, F.; Aumailley, M.; Devoulée, A.; Koteliansky, V.; Babinet, C.; Krieg, T. Impaired mechanical stability, migration and contractile capacity in vimentin-deficient fibroblasts. *J. Cell Sci.* **1998**, *111*, 1897–1907.

(52) Guo, M.; Ehrlicher, A. J.; Mahammad, S.; Fabich, H.; Jensen, M. H.; Moore, J. R.; Fredberg, J. J.; Goldman, R. D.; Weitz, D. A. The role of vimentin intermediate filaments in cortical and cytoplasmic stiffness. *Biophys. J.* **2013**, *105*, 1562–1568.

(53) Lowery, J.; Kuczmarski, E. R.; Herrmann, H.; Goldman, R. D. Intermediate filaments play a pivotal role in regulating cell architecture and function. *J. Biol. Chem.* **2015**, *290*, 17145–17153.

(54) Herrmann, H.; Kreplak, L.; Aebi, U. Isolation, characterization, and in vitro assembly of intermediate filaments. *Method Cell Biol.* **2004**, *78*, 3–24.

(55) Block, J.; Witt, H.; Candelli, A.; Danes, J. C.; Peterman, E. J. G.; Wuite, G. J. L.; Janshoff, A.; Köster, S. Viscoelastic properties of vimentin originate from nonequilibrium conformational changes. *Sci. Adv.* **2018**, *4*.

(56) Forsting, J.; Kraxner, J.; Witt, H.; Janshoff, A.; Köster, S. Vimentin intermediate filaments undergo irreversible conformational changes during cyclic loading. *Nano Lett.* **2019**, *19*, 7349–7356.

(57) Winheim, S.; Hieb, A. R.; Silbermann, M.; Surmann, E.-M.; Wedig, T.; Herrmann, H.; Langowski, J.; Mücke, N. Deconstructing the late phase of vimentin assembly by total internal reflection fluorescence microscopy (TIRFM). *PLoS One* **2011**, *6*, e19202.

(58) Nöding, B.; Köster, S. Intermediate filaments in small configuration spaces. *Phys. Rev. Lett.* **2012**, *108*, 088101.

(59) Block, J.; Witt, H.; Candelli, A.; Peterman, E. J. G.; Wuite, G. J. L.; Janshoff, A.; Köster, S. Nonlinear loading-rate-dependent force response of individual vimentin intermediate filaments to applied strain. *Phys. Rev. Lett.* **2017**, *118*, 048101.

(60) Mücke, N.; Wedig, T.; Bürer, A.; Marekov, L. N.; Steinert, P. M.; Langowski, J.; Aebi, U.; Herrmann, H. Molecular and biophysical characterization of assembly-starter units of human vimentin. *J. Mol. Biol.* **2004**, *340*, 97–114.

(61) Shelanski, M. L. Chemistry of the filaments and tubules of the brain. *J. Histochem. Cytochem.* **1973**, *21*, 529–539.

(62) Malekzadeh-Hemmat, K.; Gendry, P.; Launay, J. F. Rat pancreas kinesin: identification and potential binding. *Cell. Mol. Biol.* **1993**, *39*, 279–285.

(63) Hyman, A.; Drechsel, D.; Kellogg, D.; Salser, S.; Sawin, K.; Steffen, P.; Wordeman, L.; Mitchison, T. Preparation of modified tubulins. *Method Enzymol.* **1991**, *196*, 478–485.

(64) National Institute of Standards and Technology, Fundamental Physical Constants: Boltzman Constant. Constant stated at https://physics.nist.gov/cgi-bin/cuu/Value?kev (2020).

(65) Mücke, N.; Kreplak, L.; Kirmse, R.; Wedig, T.; Herrmann, H.; Aebi, U.; Langowski, J. Assessing the flexibility of intermediate filaments by atomic force microscopy. *J. Mol. Biol.* **2004**, *335*, 1241–1250.

(66) Thanh, V. H.; Priami, C. Simulation of biochemical reactions with time-dependent rates by the rejection-based algorithm. *J. Chem. Phys.* **2015**, *143*, 054104.

(67) Gillespie, D. T. Exact stochastic simulation of coupled chemical reactions. *J. Phys. Chem.* **1977**, *81*, 2340–2361.

(68) Erdmann, T.; Schwarz, U. S. Stability of adhesion clusters under constant force. *Phys. Rev. Lett.* **2004**, *92*, 108102.

(69) Corder, G. W.; Foreman, D. I. *Nonparametric Statistics: A Step-By-Step Approach*; John Wiley & Sons, Somerset, 2014.

(70) Tao, Y.-G.; den Otter, W. K.; Dhont, J. K. G.; Briels, W. J. Isotropic-nematic spinodals of rigid long thin rodlike colloids by event-driven Brownian dynamics simulations. *J. Chem. Phys.* **2006**, *124*, 134906.

(71) Schmidt, C. F.; Baermann, M.; Isenberg, G.; Sackmann, E. Chain dynamics, mesh size, and diffusive transport in networks of polymerized actin: a quasielastic light scattering and microfluorescence study. *Macromolecules* **1989**, *22*, 3638–3649.

(72) Kestin, J.; Sokolov, M.; Wakeham, W. A. Viscosity of Liquid Water in the Range -8°C to 150 C. *J. of Phys. Chem. Ref. Data* **1978**, *7*, 941–948.

(73) Pollard, T. D.; Earnshaw, W. C. *Cell Biology*; Springer, Berlin, Heidelberg, 2007.

(74) Granek, R. From semi-flexible polymers to membranes: anomalous diffusion and reptation. *J. Phys. II* **1997**, *7*, 1761–1788.

(75) Fees, C. P.; Moore, J. K. A unified model for microtubule rescue. *Mol. Biol. Cell* **2019**, *30*, 753–765.

(76) Sigma Aldrich Product Information Methyl Cellulose. https://www.sigmaaldrich.com/, accessed (2020).

(77) Herrmann, H.; Häner, M.; Brettel, M.; Müller, S. A.; Goldie, K. N.; Fedtke, B.; Lustig, A.; Franke, W. W.; Aebi, U. Structure and assembly properties of the intermediate filament protein vimentin: the role of its head, rod and tail domains. *J. Mol. Biol.* **1996**, *264*, 933–953.